Research Square

Preprints are preliminary reports that have not undergone peer review.
They should not be considered conclusive, used to inform clinical practice,
or referenced by the media as validated information.

A New Generated Class: Theory and Inference with Application to Daily COVID-19 Cases in Region Aseer, Saudi Arabia

Muhammad Arshad

vf_mzeshanarsha@brocku.ca

Brock University

Ali Algarni

King Abdulaziz University

Research Article

Keywords: Generated Family, Weibull distribution, Shannon Entropy, Inference, COVID-19, Saudi Arabia

Posted Date: August 27th, 2026

DOI: https://doi.org/10.21203/rs.3.rs-8475376/v1

License: This work is licensed under a Creative Commons Attribution 4.0 International License.
Read Full License

Additional Declarations: No competing interests reported.

A New Generated Class: Theory and Inference with Application to Daily COVID-19 Cases in Region Aseer, Saudi Arabia

Muhammad Zeshan Arshad[1], Ali Algrani[2]
[1]Department of Mathematics and Statistics, Brock University, St. Catharines, ON, Canada
[2]Faculty of Science, Department of Mathematics and Statistics, King Abdulaziz University, Jaddah, Saudi Arabia
[1]Corresponding Author Email: vf_mzeshanarsha@brocku.ca
[2]Email: ahalgarni@kau.edu.sa

Abstract: This paper develops a trigonometric-generated (T–G) family of distributions for heterogeneous outbreak data and studies a parsimonious Weibull-baseline special case, the NewWeibull distribution. We derive closed-form moment expressions via a Maclaurin expansion of the generator, establish conditions for valid series–integral interchange, and provide regularity results for maximum likelihood estimation, yielding identifiability and large-sample behavior of the shape (k) and scale (η) parameters. A Monte Carlo study across sample sizes $n = 50 - 2000$ evaluates finite-sample performance: the estimator of η is effectively unbiased with variance shrinking at the expected rate; the estimator of k exhibits a small positive bias only at very small n, which dissipates rapidly; and mean-squared errors decrease monotonically for both parameters. Applied to daily COVID-19 case distributions from five urban centers in Saudi Arabia's Aseer Region, the NewWeibull distribution achieves lower Anderson–Darling and Cramér–von Mises statistics while maintaining high Kolmogorov–Smirnov p-values, outperforming Weibull, Gamma, LogNormal, Exponential, Exponentiated-Exponential, and SinWeibull alternatives. Overall, the T–G framework is flexible yet analytically tractable, and its NewWeibull distribution special case is mathematically sound, simulation-validated, and empirically effective for outbreak modeling.

Keywords: Generated Family, Weibull distribution, Shannon Entropy, Inference, COVID-19, Saudi Arabia

1. Introduction

Developing flexible probability models that can manage data with irregular or extreme behavior remains a central challenge in applied statistics. Such data frequently arise in fields as diverse as reliability engineering (Sindhu and Atangana [1]), healthcare survival analysis (Liu et al. [2]), financial risk modeling (Shen et al.[3]), hydrological extremes (Moccia et al. [4]), time-to-event and system reliability studies (Chen and Ye, [5]; Xu et al. [6]), and lifetime performance evaluation (Zhang et al. [7]; Luo et al. [8]; Zhuang et al. [9]).

Classical distributions often fall short in these contexts because they cannot adequately capture extreme values or heavy-tailed features that dominate real-world data. The existing literature demonstrates that heavy-tailed (HT) models provide superior fits when such anomalies are present, since they better reflect rare but high-impact observations. Nonetheless, only a limited number of probability models naturally embody HT properties. As a result, there is a continuing need to design new distribution families that combine analytical tractability with the flexibility required to accommodate datasets marked by heavy tails and extreme fluctuations.

To enhance the flexibility of conventional models, several new generated (G) distribution families have been proposed in recent years. For example, the truncated Burr X generated (TrBrX-G) family of distributions introduced by Bantan et al. [10] has shown promising results for actuarial and financial data. Similarly, the Fréchet Topp–Leon generated (FréTG) family of distributions developed by Reyad et al. [11] extends the baseline flexibility of classical models through novel characterizations and applications. Eghwerido and Agu [12] proposed the shifted Gompertz generated (SG-G) family of distributions, while Eghwerido et al. [13] later advanced the Teissier generated (Tei-G) family of distributions, both of which expanded the scope of G distributions and demonstrated applicability in different real-world contexts. More recently, Altun et al. [14] introduced the Gudermannian-generated (Gud-G) family of distributions, offering regression modeling capacity and multiple characterizations.

Parallel to these efforts, Kumar et al. [15] suggested a sine-function-based distribution, which has been applied in biomedical studies such as bladder cancer data modeling. The alpha-generated (Alpha-G) class improved forecasting and policy design in cross-country settings (Alharbi, 2024 [16]).

1.1. COVID-19 Global Influence

COVID-19 required probability models that manage skewed, heavy-tailed epidemic data. Classical Gaussian and log-normal forms often miss key features of outbreak curves (Gonçalves et al. [17]), so researchers turned to Weibull-type extensions and generated families. The NMFWE distribution improved mortality prediction for Mexico and Canada (Ahmad et al. [18]). In South Asia, the NFW distribution modeled mortality in Pakistan and Afghanistan (Farooq et al. [19]), and the standard Weibull distribution fit case data in Pakistan (Haq et al. [20]). For North America and Europe, the GW distribution captured Canadian mortality (Xin et al. [21]), the EExW distribution fit deaths in Canada and the Netherlands (Arif et al. [22]).

Beyond Weibull forms, alternative distributions addressed specific facets of the pandemic: the DWQL distribution tracked vaccination uptake in North America and the Arabian Peninsula (Ahmadini et al. [23]); the ELx distribution was fitted to infection data (Alsuhabi et al. [24]); the IPHaq distribution modeled mortality in Kuwait (BuHamra et al. [25]); the PHaq distribution analyzed Chinese patient data (Tashkandy et al. [26]); and the PBilal distribution described spread in Saudi Arabia and the Netherlands (Riad et al. [27]). Early cases in Pakistan were studied using the EMIExEx distribution (Bantan et al. [28]), and the TIHLBrW distribution supported pandemic applications (Alshanbari et al. [29]). Discrete formulations managed counts data (Almetwally et al. [30]) and mortality (Aljohani et al. [31]), while population-level excess mortality for 2020–2021 was examined by Raihen et al. [32].

To develop more understanding of trigonometric models, see the work of Faruk et al. [33], Elbatal et al. [34], Ogumeyo et al. [35], Kumar et al. [36], Mahmood et al. [37], and Tashkandy et al. [38]

Localized COVID-19 outbreaks in small and semi-urban settings display features strong right-skew, heavy tails, and shifting hazard shapes that strain classical distributions such as Weibull, Gamma, LogNormal, and Exponential. The Aseer Region of Saudi Arabia exemplifies this problem: complex topography, altitude gradients, and uneven population density generate daily case series with nonstandard shape and volatility. What is needed is a framework that preserves parsimony and closed forms while flexibly capturing these behaviors and supporting rigorous inference.

To meet this need, we develop a trigonometric-generated (T–G) family of distributions and study its Weibull-baseline special case, the NewWeibull distribution. The new family yields PDF, CDF, survival, hazard, and moment expressions without introducing extra parameters. We establish conditions that justify the moment calculus and maximum-likelihood regularity, giving identifiability and large-sample properties for the shape k and scale η. A Monte Carlo investigation over realistic sample sizes examines finite-sample performance, showing that $\hat{\eta}$ is unbiased with shrinking variance and that the small-sample bias of $\hat{k}$ dissipates rapidly; practical guidance on window lengths follows.

The empirical component analyzes daily COVID-19 case distributions from five Aseer cities. Using complementary criteria the KS statistic (with p-value), ADE, and CVME, we find consistent gains for NewWeibull distribution relative to classical and alternative models.

This study positions the T–G framework and its NewWeibull distribution special case as a parsimonious, analytically tractable, and empirically strong approach for outbreak modeling in underrepresented regions, bridging mathematical development, simulation evidence, and multi-city validation.

2. Methodology

2.1. Construction of T–G Family

Souza [39] introduced the trigonometric generated family with continuous cumulative distribution function (CDF) denoted by $P_{X|(x;\theta)}$

$$P_{X|(x;\theta)} = sin\left(\frac{\pi}{2}G(x;\theta)\right)$$

Motivated by this idea, we proposed a new trigonometric generator (T–G) model with CDF is defined as

$$F_{X|(x;\theta)} = \frac{2\,G(x;\theta)}{1 + sin\left(\frac{\pi}{2}G(x;\theta)\right)}. \tag{1}$$

It is straightforward to check that $F_{X|(-\infty)} = 0$ and $F_{X|(+\infty)} = 1$, ensuring the validity of the distribution. Differentiating Equation (1) with respect to x, to get the PDF presented as:

$$f_{X|(x;\theta)} = \frac{2\,g(x;\theta)\left[1 + sin\left(\frac{\pi}{2}G(x;\theta)\right) - \frac{\pi}{2}G(x;\theta)cos\left(\frac{\pi}{2}G(x;\theta)\right)\right]}{\left[1 + sin\left(\frac{\pi}{2}G(x;\theta)\right)\right]^2}. \tag{2}$$

The survival, hazard rate, and cumulative hazard functions are expressed respectively as:

$$\bar{F}_{X|(x;\theta)} = 1 - F_{X|(x;\theta)} = \frac{1 + sin\left(\frac{\pi}{2}G(x;\theta)\right) - 2G(x;\theta)}{1 + sin\left(\frac{\pi}{2}G(x;\theta)\right)}, \tag{3}$$

$$hr_{X|(x;\theta)} = \frac{f_{X|(x;\theta)}}{\bar{F}_{X|(x;\theta)}} = \frac{2\,g(x;\theta)\left[1 + sin\left(\frac{\pi}{2}G(x;\theta)\right) - \frac{\pi}{2}G(x;\theta)cos\left(\frac{\pi}{2}G(x;\theta)\right)\right]}{\left[1 + sin\left(\frac{\pi}{2}G(x;\theta)\right)\right]\left[1 + sin\left(\frac{\pi}{2}G(x;\theta)\right) - 2G(x;\theta)\right]}, \tag{4}$$

$$\Lambda_{X|(x;\theta)} = -\,ln\left(\frac{1 + sin\left(\frac{\pi}{2}G(x;\theta)\right) - 2G(x;\theta)}{1 + sin\left(\frac{\pi}{2}G(x;\theta)\right)}\right).$$

2.2. Moments and Related Measures

Let X ~T-G $(G, g; \theta)$on support $S \subset (0, \infty)$. For any $r \geq 0$ such that the integral exists, the r-th raw moment is

$$m_r(\theta) = \mathbb{E}[X^r] = \int_S x^r\, f(x;\theta)\, dx. \tag{5}$$

Using the T–G density $f(x;\theta) = g(x;\theta)\, H'\big(G(x;\theta)\big)$, we get

$$m_r(\theta) = \int_S x^r\, g(x;\theta)\, H'\big(G(x;\theta)\big) dx, \tag{6}$$

For proposed T-G family the Maclaurin expansion about $u = 0$

$$H'(u) = \sum_{m\geq 1} c_m u^{\,m-1}, \tag{7}$$

$$c_1 = 2, \quad c_2 = -2\pi, \quad c_3 = \frac{3}{2}\pi^2, \quad c_4 = -\frac{5}{6}\pi^3, c_5 = \frac{5}{12}\pi^4, \quad c_6 = -\frac{61}{320}\pi^5, \ldots .$$

This series has radius of convergence equal to 1, since the nearest singularity of $1 + sin\left(\frac{\pi}{2}u\right)$ occurs at $u = -1$. Hence it converges uniformly on $[0, \rho]$ for any $\rho \in (0,1)$. Substituting Equation (7) into Equation (6) gives

$$m_r(\theta) = \sum_{m=1}^{\infty} c_m \int_S x^r\, g(x;\theta)\, G(x;\theta)^{\,m-1}\, dx \;=\; \sum_{m\geq 1} c_m\; M_{r,m-1}(\theta), \tag{8}$$

where

$$M_{r,s}(\theta) = \mathbb{E}[X^r\, G(X;\theta)^s] = \int_S x^r\, g(x;\theta)\, G(x;\theta)^s dx$$

is probability weighted moment (PWM) type functional.

2.3. Shannon Entropy

Let a baseline CDF/PDF be $G(x;\theta)$ and $g(x;\theta)$ on support $S \subseteq R$. Let $H:[0,1] \to [0,1]$ be differentiable, strictly increasing, with $H(0) = 0, H(1) = 1$. The T–G model with CDF $F_{X|(x;\theta)}$ and PDF $f_{X|(x;\theta)}$ is presented as

$$F_{X|(x;\theta)} = H\big(G(x;\theta)\big), \tag{9}$$

$$f_{X|(x;\theta)} = g(x;\theta)\, H'\big(G(x;\theta)\big). \tag{10}$$

Assumptions

a) $H'$is continuous and positive on $[0,1]$;

b) g is a proper density on S;

c) $\int_S f_{X|(x;\theta)} \left|ln\, f_{X|(x;\theta)}\right| dx < \infty$.

The Shannon entropy is defined as:

$$\mathcal{H}_{X|(x;\theta)} = -\int_S f_{X|(x;\theta)}\, ln f_{X|(x;\theta)}\, dx. \tag{11}$$

Substituting Equation (2) and splitting into two contributions yields the T–G family of distributions.

$$\mathcal{H}_{X|(x;\theta)} = -\int_S g(x;\theta) H'\big(G(x;\theta)\big)\, ln\, g\,(x;\theta)\, dx - \int_S g(x;\theta) H'\big(G(x;\theta)\big)\, ln\, H'\,\big(G(x;\theta)\big)\, dx. \tag{12}$$

2.4. Order Statistics

If $X_1, X_2, \dots, X_n$ are i.i.d. observations from the T–G family of distributions, the CDF$F_{X|r:n}$ and PDF $f_{X|r:n}$of the rth order statistic (OS) is presented by

$$F_{X|r:n} = \sum_{j=r}^{n} \binom{n}{j} \left[F_{X|(x;\theta)}\right]^j \left[1 - F_{X|(x;\theta)}\right]^{n-j}, \tag{13}$$

$$f_{X|r:n} = \frac{n!}{(r-1)!\,(n-r)!} \left[F_{X|(x;\theta)}\right]^{r-1} \left[1 - F_{X|(x;\theta)}\right]^{n-r} f_{X|(x;\theta)}. \tag{14}$$

With reference to Equations (1−3), the rth OS CDF and PDF are presented as:

$$F_{X|r:n} = Pr(X_{r:n} \le x) \tag{13a}$$

$$= \sum_{j=r}^{n} \binom{n}{j} \left[\frac{2\,G(x;\theta)}{1 + sin\left(\frac{\pi}{2} G(x;\theta)\right)}\right]^j \left[\frac{1 + sin\left(\frac{\pi}{2} G(x;\theta)\right) - 2\,G(x;\theta)}{1 + sin\left(\frac{\pi}{2} G(x;\theta)\right)}\right]^{n-j},$$

$$f_{X|r:n} \tag{14a}$$

$$= \left[\frac{n!}{(r-1)!\,(n-r)!} \left[\frac{2\,G(x;\theta)}{1 + sin\left(\frac{\pi}{2} G(x;\theta)\right)}\right]^{r-1} \left[\frac{1 + sin\left(\frac{\pi}{2} G(x;\theta)\right) - 2\,G(x;\theta)}{1 + sin\left(\frac{\pi}{2} G(x;\theta)\right)}\right]^{n-r} \times \left[\frac{2\,g(x;\theta)\left[1 + sin\left(\frac{\pi}{2} G(x;\theta)\right) - \frac{\pi}{2} G(x;\theta) cos\left(\frac{\pi}{2} G(x;\theta)\right)\right]}{\left[1 + sin\left(\frac{\pi}{2} G(x;\theta)\right)\right]^2}\right]\right].$$

2.5. Inference

For i.i.d. sample $x_1, \dots, x_n$from the T–G family of distributions, the log-likelihood ($\ell_{X|(x;\theta)}$) is presented as:

$$\ell_{X|(x;\theta)} = \sum_{i=1}^{n} ln f_{X|(x;\theta)} = \sum_{i=1}^{n} \big[ln\, g\,(x_i;\theta) + ln\, H'\,\big(G(x_i;\theta)\big)\big]. \tag{15}$$

For any parameter θ_j, score function

$$\frac{\partial l(\theta)}{\partial \theta_j} = \sum_{i=1}^{n} \left[\frac{\partial}{\partial \theta_j} ln\, g_i(x_i;\theta) + \frac{H'' G_i(x_i;\theta)}{H' G_i(x_i;\theta)} \times \frac{\partial G_i(x_i;\theta)}{\partial \theta_j} \right], \tag{16}$$

and for observed information matrix, the second derivatives are

$$\frac{\partial^2 l}{\partial \theta_j \partial \theta_k} = \sum_{i=1}^{n} \left[\begin{array}{c} \frac{\partial^2}{\partial \theta_j \partial \theta_k} ln\, g_i(x_i;\theta) + D'_G G_i(x_i;\theta)\, \frac{\partial G_i(x_i;\theta)}{\partial \theta_j} \frac{\partial G_i(x_i;\theta)}{\partial \theta_k} + \\ D_G G_i(x_i;\theta)\, \frac{\partial^2 G_i(x_i;\theta)}{\partial \theta_j \partial \theta_k} \end{array} \right], \tag{17}$$

where

$$D_G G_i(x_i;\theta) = \frac{H'' G_i(x_i;\theta)}{H' G_i(x_i;\theta)}, \qquad D'_G G_i(x_i;\theta) = \frac{d}{dG_i(x_i;\theta)} \left(\frac{H'' G_i(x_i;\theta)}{H' G_i(x_i;\theta)} \right). \tag{18}$$

3. Statistical Properties

3.1. NewWeibull Distribution

Let the CDF $G_{X|(\eta,k)}$and PDF $g_{X|(\eta,k)}$of the baseline Weibull~$(\eta, k)$with $\eta > 0,\ k > 0$ are presented as:

$$G_{X|(\eta,k)} = 1 - e^{-\left(\frac{x}{\eta}\right)^k}, \tag{19}$$

$$g_{X|(\eta,k)} = \frac{k}{\eta} \left(\frac{x}{\eta}\right)^{k-1} e^{-\left(\frac{x}{\eta}\right)^k}, \tag{20}$$

respectively. The NewWeibull distribution CDF $F_{X|(\eta,k)}$and PDF $f_{X|(\eta,k)}$with reference to Equations (1) and (2) are presented as:

$$F_{X|(\eta,k)} = \frac{2\left(1 - e^{-\left(\frac{x}{\eta}\right)^k}\right)}{1 + sin\left(\frac{\pi}{2}\left[1 - e^{-\left(\frac{x}{\eta}\right)^k}\right]\right)}, \tag{21}$$

$$f_{X|(\eta,k)} = \frac{2\,\frac{k}{\eta}\left(\frac{x}{\eta}\right)^{k-1} e^{-\left(\frac{x}{\eta}\right)^k} \left[\begin{array}{c} 1 + sin\left(\frac{\pi}{2}\left[1 - e^{-\left(\frac{x}{\eta}\right)^k}\right]\right) - \\ \frac{\pi}{2}\left[1 - e^{-\left(\frac{x}{\eta}\right)^k}\right] cos\left(\frac{\pi}{2}\left[1 - e^{-\left(\frac{x}{\eta}\right)^k}\right]\right) \end{array} \right]}{\left[1 + sin\left(\frac{\pi}{2}\left[1 - e^{-\left(\frac{x}{\eta}\right)^k}\right]\right)\right]^2}, \tag{22}$$

3.2. Reliability Measure

The reliability measures that significantly contribute including survival $\bar{F}_{X|(\eta,k)}$, and hazard rate $H_{X|(\eta,k)}$ functions are presented by

$$\bar{F}_{X|(\eta,k)} = 1 - F_{X|(\eta,k)} = \frac{1 + sin\left(\frac{\pi}{2}\left[1 - e^{-\left(\frac{x}{\eta}\right)^k}\right]\right) - 2\left(1 - e^{-\left(\frac{x}{\eta}\right)^k}\right)}{1 + sin\left(\frac{\pi}{2}\left[1 - e^{-\left(\frac{x}{\eta}\right)^k}\right]\right)}, \tag{23}$$

$$hr_{X|(\eta,k)} = \frac{f_{X|(\eta,k)}}{\bar{F}_{X|(\eta,k)}} = \frac{2\,\frac{k}{\eta}\left(\frac{x}{\eta}\right)^{k-1} e^{-\left(\frac{x}{\eta}\right)^{k}} \left[\begin{array}{c} 1+sin\left(\frac{\pi}{2}\left[1-e^{-\left(\frac{x}{\eta}\right)^{k}}\right]\right)- \\ \frac{\pi}{2}\left[1-e^{-\left(\frac{x}{\eta}\right)^{k}}\right] cos\left(\frac{\pi}{2}\left[1-e^{-\left(\frac{x}{\eta}\right)^{k}}\right]\right) \end{array}\right]}{\left[\begin{array}{c} \left[1+sin\left(\frac{\pi}{2}\left[1-e^{-\left(\frac{x}{\eta}\right)^{k}}\right]\right)\right]\times \\ \left[1+sin\left(\frac{\pi}{2}\left[1-e^{-\left(\frac{x}{\eta}\right)^{k}}\right]\right)-2\left(1-e^{-\left(\frac{x}{\eta}\right)^{k}}\right)\right] \end{array}\right]}, \tag{24}$$

3.3. Asymptotic Properties

Let $X\sim$ NewWeibull(k,η) with CDF $F_{X|(\eta,k)}$ and PDF $f_{X|(\eta,k)}$given in Equations (21)–(22), survival and hazard rate functions in Equations (23)– (24). Denote by

$$c_0 \coloneqq G'(0^+), \qquad c_1 \coloneqq G'(1^-),$$

where $G(\cdot)$ is the trigonometric generator function.

Proposition 1 (PDF Limiting Behavior).

As $x \to 0^+$,

$$f_{X|(\eta,k)} \sim c_0\,\frac{k}{\eta}\left(\frac{x}{\eta}\right)^{k-1}.$$

Hence,

a) if $k < 1$, then $f_{X|(\eta,k)} \to \infty$;
b) if $k = 1$, then $f_{X|(\eta,k)} \to c_0/\eta$;
c) if $k > 1$, then $f_{X|(\eta,k)} \to 0$

As $x \to \infty$,

$$f_{X|(\eta,k)} \to 0.$$

Proposition 2 (HRF Limiting Behavior).

As $x \to 0^+$,

$$hr_{X|(\eta,k)} \sim c_0\,\frac{k}{\eta}\left(\frac{x}{\eta}\right)^{k-1}.$$

Thus, the hazard exhibits the same trichotomy near the origin as the density.

As $x \to \infty$,

$$hr_{X|(\eta,k)} \sim \frac{k}{\eta}\left(\frac{x}{\eta}\right)^{k-1}.$$

Therefore,

a) if $k < 1$, then $hr_{X|(\eta,k)} \to 0$;
b) if $k = 1$, then $hr_{X|(\eta,k)} \to 1/\eta$;
c) if $k > 1$, then $hr_{X|(\eta,k)} \to \infty$.

3.4. Moments

The r-th raw moments and shape measures for $r \geq 0$,

$$\mathbb{E}_{X^r|(\eta,k)} = \int_0^\infty x^r f_{X|(\eta,k)} dx\,. \tag{25}$$

Reference to Equation (22), shorthand's are introduced for the simplify the calculations such as:

$$S(x;\eta,k) = sin(\frac{\pi}{2}G(x;\eta,k)), \qquad C(x;\eta,k) = cos(\frac{\pi}{2}G(x;\eta,k)), \qquad g(x;\eta,k) = \partial x G(x;\eta,k),$$

$$f_{X|(\eta,k)} = \frac{2\,g(x;\eta,k)\left[\,1+S(x;\eta,k)-\frac{\pi}{2}G(x;\eta,k)C(x;\eta,k)\right]}{[1+S(x)\,]^2}. \tag{26}$$

Insert Equation (26) and the Weibull $g(x;\eta,k)$ from Equations (19) and (20):

$$\mathbb{E}_{X^r|(\eta,k)} \tag{27}$$
$$= \int_0^\infty x^r\,\frac{k}{\eta}\left(\frac{x}{\eta}\right)^{k-1} e^{-(x/\eta)^k}\,\frac{2\,g(x;\eta,k)\left[\,1+S(x;\eta,k)-\frac{\pi}{2}G(x;\eta,k)C(x;\eta,k)\right]}{[1+S(x;\eta,k)\,]^2}dx.$$

Let's suppose

$$t = \left(\frac{x}{\eta}\right)^k \Rightarrow x = \eta\,t^{\frac{1}{k}},\; dx = \frac{\eta}{k}t^{\frac{1}{(k-1)}}dt.$$

Then

$$g(x;\eta,k)\,dx = \frac{k}{\eta}\left(\frac{x}{\eta}\right)^{k-1} e^{-t}\,dx = \frac{k}{\eta}\,t^{\frac{(k-1)}{k}}e^{-t}\,\eta\,\frac{1}{k}t^{\frac{1}{(k-1)}}dt = e^{-t}\,dt.$$

Also $G(x;\eta,k) = 1-e^{-t}$. Therefore Equation (28) becomes.

$$\mathbb{E}_{X^r|(\eta,k)} = \eta^r\int_0^\infty t^{\frac{r}{k}}\,H'(1-e^{-t})dt, \tag{28}$$

where

$$H'(y) = \frac{2\left[1+sin\left(\frac{\pi}{2}y\right)-\frac{\pi}{2}y\,cos\left(\frac{\pi}{2}y\right)\right]}{\left[1+sin\left(\frac{\pi}{2}y\right)\right]^2}. \tag{29}$$

Use the Maclaurin series (about $y=0$) in powers of y:

$$H'(y) = \sum_{m\geq 1} c_m\,y^{\,m-1}, c_1 = 2,\; c_2 = -2\pi,\; c_3 = \frac{3}{2}\pi^2,\; c_4 = -\frac{5}{6}\pi^3, \tag{30}$$
$$c_5 = \frac{5}{12}\pi^4,\; c_6 = -\frac{61}{320}\pi^5, \ldots$$

and set $y = 1-e^{-t}$. Then

$$H'(1-e^{-t}) = \sum_{m\geq 1} c_m\,(1-e^{-t})^{m-1}. \tag{31}$$

Binomial expansion simplifies.

$$(1-e^{-t})^{m-1} = \sum_{j=0}^{m-1}(-1)^j\binom{m-1}{j}e^{-jt}. \tag{32}$$

Insert Equations (31)– (32) into Equation (28), exchange sum/integral (absolute convergence on compact ranges), and use

$$\int_0^\infty t^{\,r/k}\;e^{-(1+j)t}\,dt = \frac{\Gamma(1+r/k)}{(1+j)^{\,1+r/k}}. \tag{33}$$

Hence

$$\mu_r = \mathbb{E}_{X^r|(\eta,k)} = \eta^r\sum_{m=1}^{\infty} c_m\sum_{j=0}^{m-1}\frac{(-1)^j\binom{m-1}{j}}{(1+j)^{\,1+\frac{r}{k}}}\Gamma\left(1+\frac{r}{k}\right). \tag{34}$$

The 1st four central moments for X

$$\mu_2 = m_2-\mu^2,\quad \mu_3 = m_3-3\mu m_2+2\mu^3,\quad \mu_4 = m_4-4\mu m_3+6\mu^2 m_2-3\mu^4,$$

and standardized shape measures are defined as:

$$\gamma_1 = \mu_3/\mu_2^{3/2},\qquad excess\,\gamma_2 = \mu_4/\mu_2^2-3.$$

For $t>0$, moment generating function $E_{e^{tX}|(\eta,k)}$ of X is defined as:

$$\mathbb{E}_{e^{tX}|(\eta,k)} = \sum_{r=0}^{\infty}\frac{t^r}{r!}\mathbb{E}_{X^r|(\eta,k)} = \sum_{r=0}^{\infty}\frac{t^r}{r!}\eta^r\sum_{m=1}^{\infty}c_m\sum_{j=0}^{m-1}\frac{(-1)^j\binom{m-1}{j}}{(1+j)^{\,1+\frac{r}{k}}}\Gamma\left(1+\frac{r}{k}\right).$$

For $t > 0$, characteristic function $E_{e^{itX}|(\eta,k)}$ of X is defined as:

$$\mathbb{E}_{e^{itX}|(\eta,k)} = \sum_{r=0}^{\infty} \frac{(it)^r}{r!} \mathbb{E}_{X^r|(\eta,k)} = \sum_{r=0}^{\infty} \frac{(it)^r}{r!} \eta^r \sum_{m=1}^{\infty} c_m \sum_{j=0}^{m-1} \frac{(-1)^j \binom{m-1}{j}}{(1+j)^{1+\frac{r}{k}}} \Gamma\left(1+\frac{r}{k}\right).$$

The r-th lower incomplete moment $(m_r(t))$ for $r > -1$and $t > 0$ is defined as

$$m_r(t) = \mathbb{E}[X^r|_{X \le t}] = \int_0^t x^r f_{X|(\eta,k)}\, dx, \tag{35}$$

Then

$$m_r(t) = \eta^r \int_0^{(t/\eta)^k} y^{\frac{r}{k}} \phi(y) dy, \tag{35a}$$

where $\phi(y)$ denotes the link–density kernel obtained by rewriting $f_{X|(\eta,k)}dx$ under y.To obtain computable closed forms, expand the trigonometric link terms about e^{-y} exactly as in the moment section (Maclaurin / binomial steps used around Equations (30)−(34). This yields the convergent series representation

$$\phi(y) = \sum_{j=0}^{\infty} \omega_j\, e^{-(j+1)y}, \qquad y \ge 0, \tag{35b}$$

with coefficients $\omega_j\big|_{j\ge 0}$ determined by the link expansion (collecting constants from the sine/cosine terms and the rational factor). Substituting Equations (35b) and (35a) and Equation (35) gives

$$m_r(t) = \eta^r \sum_{j=0}^{\infty} \omega_j \int_0^{(t/\eta)^k} y^{\frac{r}{k}} e^{-(j+1)y}\, dy,$$

$$m_r(t) = \eta^r \sum_{j=0}^{\infty} \omega_j\, (j+1)^{-\left(1+\frac{r}{k}\right)} \Gamma\left(1+\frac{r}{k}, (j+1)\left(\frac{t}{\eta}\right)^k\right), \tag{35c}$$

where $\gamma(0,b)$is the lower incomplete gamma function.

For 1st and 2nd incomplete moments, set $(r = 1,2)$ in Equation (35c) are given by

$$m_1(t) = \eta \sum_{j=0}^{\infty} \omega_j\, (j+1)^{-\left(1+\frac{1}{k}\right)} \Gamma\left(1+\frac{1}{k}, (j+1)\left(\frac{t}{\eta}\right)^k\right), \tag{35d}$$

$$m_2(t) = \eta^2 \sum_{j=0}^{\infty} \omega_j\, (j+1)^{\left(1+\frac{2}{k}\right)} \Gamma\left(1+\frac{2}{k}, (j+1)\left(\frac{t}{\eta}\right)^k\right). \tag{35e}$$

The corresponding upper tail incomplete moments can be derived by following Equations (34) and (35c) as

$$\mathbb{E}[\, X^r|_{X>t}] = \mu_r - m_r(t).$$

3.5. Numerical and Graphical Analysis

The numerical summaries in Tables 1–2 and the heatmaps in Figures 1–3 convey a consistent message: the scale parameter η amplifies magnitude uniformly, whereas the shape parameter k governs tail weight and asymmetry. This is visible row-wise in both tables—larger η increases all reported moments—and horizontally in the heatmaps, where moving to the right (larger k) progressively cools the color intensity.

For the *raw moments* (Table 1; Figure 2), scaling by η is evident. At $k = 2$, m_1 moves from 0.400 at $\eta = 0.5$ to 0.800 at $\eta = 1$ and 1.601 at $\eta = 2$, and m_4 climbs from 0.113 to 1.816 to 29.051 over the same η sequence, matching the expected η^r behavior. Holding η fixed, increasing k sharply reduces higher moments, signaling lighter tails: for $\eta = 1$, m_4 falls from 419.815 at $k = 0.7$ to 23.243 at $k =$

1, to 3.742 at $k = 1.5$, to 1.816 at $k = 2$, and to 1.054 at $k = 3$. The rightward fade in the raw moment heatmap reproduces this contraction.

Central moments follow the same pattern (Table 2; Figure 1). The variance μ_2 decreases monotonically in k for every η; at $\eta = 2$ it drops from 13.837 ($k = 0.7$) to 4.152 ($k = 1$), 1.632 ($k = 1.5$), 0.965 ($k = 2$), and 0.496 ($k = 3$). The fourth central moment illustrates the tail thinning even more starkly: with $\eta = 1, \mu_4$ moves from 287.847 at $k = 0.7$ to 0.039 at $k = 3$. These declines appear as a strong cooling from left to right in the $\mu_2 - \mu_4$ panels.

Shape measures depend primarily on k and are invariant in η within each k column (Table 2; Figure 3). At $k = 0.7$ the distribution is highly right-skewed and heavy-tailed with $\gamma_1 \approx 3.60$ and excess $\gamma_2 \approx 21.05$. Moving to $k = 1$ yields $\gamma_1 \approx 2.11$and excess $\gamma_2 \approx 6.22$; at $k = 1.5$ this decline to about 1.20 and 1.44; at $k = 2$ to 0.769 and 0.196; and at $k = 3$ to 0.325 and −0.463, indicating mild skew with platykurtic tails. The flattening of both metrics with increasing k is clearly visible in the shape-measure heatmap.

Collectively, η controls overall scale, while k dictates form: low k produces large moments, high variance, pronounced skewness and high kurtosis; high k compresses the moment structure and approaches mesokurtic or platykurtic behavior. The figures corroborate the exact values reported in the tables and provide an immediate visual summary of these effects.

Table 1. First four raw moments metrics with parameter combinations (k, η).

k	η	m_1	m_2	m_3	m_4
0.7	0.5	0.562060914	1.180723641	4.530939109	26.23843702
	1	1.124121827	4.722894565	36.24751287	419.8149924
	1.5	1.686182741	10.62651277	122.3353559	2125.313399
	2	2.248243654	18.89157826	289.9801029	6717.039878
1	0.5	0.440950495	0.453926757	0.707726013	1.452664276
	1	0.88190099	1.815707027	5.661808107	23.24262842
	1.5	1.322851485	4.085340812	19.10860236	117.6658064
	2	1.76380198	7.26282811	45.29446485	371.8820548
1.5	0.5	0.402053508	0.263624947	0.226963378	0.233884796
	1	0.804107016	1.054499789	1.815707027	3.742156741
	1.5	1.206160524	2.372624526	6.128011218	18.9446685
	2	1.608214033	4.217999157	14.52565622	59.87450785
2	0.5	0.400194305	0.220475248	0.14790718	0.113481689
	1	0.800388609	0.88190099	1.183257439	1.815707027
	1.5	1.200582914	1.984277228	3.993493856	9.192016827
	2	1.600777219	3.527603961	9.46605951	29.05131244
3	0.5	0.41233016	0.201026754	0.110237624	0.065906237
	1	0.824660321	0.804107016	0.88190099	1.054499789
	1.5	1.236990481	1.809240787	2.976415842	5.338405184
	2	1.649320642	3.216428065	7.055207922	16.87199663

Table 2. Central moments and shape metrics with parameter combinations (k, η).

k	η	μ_2	μ_3	μ_4	γ_1	Excess-γ_2
0.7	0.5	0.864811171	2.895147387	17.99041179	3.599885948	21.05462123
	1	3.459244683	23.16117909	287.8465887	3.599885948	21.05462123
	1.5	7.783300537	78.16897944	1457.223355	3.599885948	21.05462123

	2	13.83697873	185.2894328	4605.545419	3.599885948	21.05462123
1	0.5	0.259489418	0.278722811	0.620519961	2.108594336	6.215448005
	1	1.037957671	2.229782486	9.928319369	2.108594336	6.215448005
	1.5	2.33540476	7.525515889	50.2621168	2.108594336	6.215448005
	2	4.151830684	17.83825989	158.8531099	2.108594336	6.215448005
1.5	0.5	0.101977924	0.038970879	0.046174954	1.196688056	1.440114175
	1	0.407911696	0.311767035	0.738799262	1.196688056	1.440114175
	1.5	0.917801315	1.052213743	3.740171265	1.196688056	1.440114175
	2	1.631646783	2.494136281	11.8207882	1.196688056	1.440114175
2	0.5	0.060319766	0.011394988	0.011627827	0.769173638	0.195797601
	1	0.241279064	0.091159902	0.186045233	0.769173638	0.195797601
	1.5	0.542877895	0.30766467	0.941853991	0.769173638	0.195797601
	2	0.965116257	0.729279218	2.976723725	0.769173638	0.195797601
3	0.5	0.031010593	0.001775025	0.002439345	0.325041827	-0.463393138
	1	0.124042372	0.014200196	0.039029527	0.325041827	-0.463393138
	1.5	0.279095336	0.047925662	0.197586979	0.325041827	-0.463393138
	2	0.496169487	0.113601569	0.624472429	0.325041827	-0.463393138

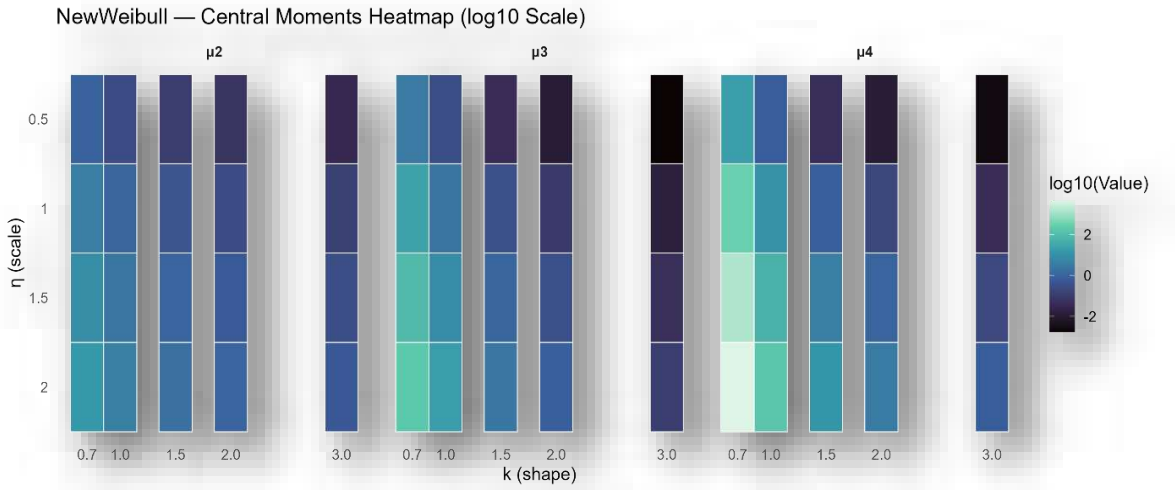

Figure 1. Central Moments Heatmap.

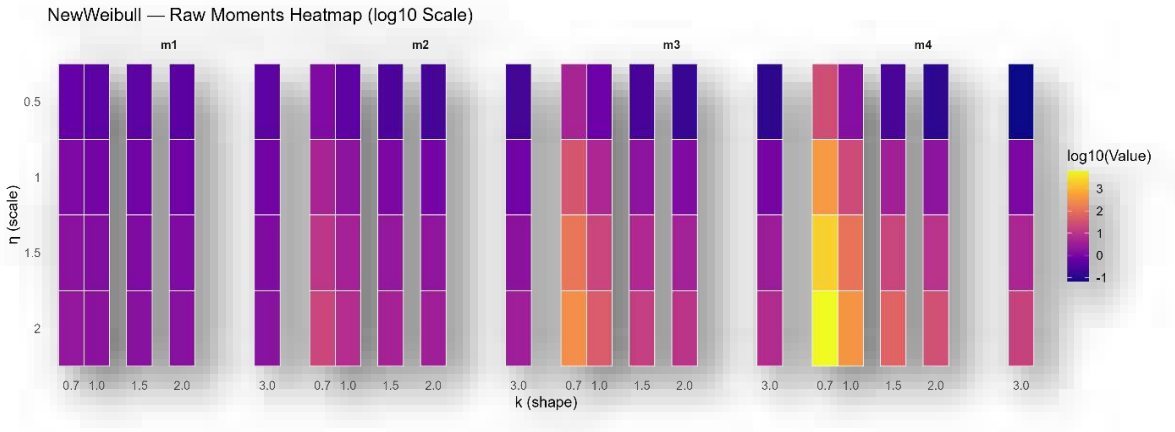

Figure 2. Raw Moments Heatmap.

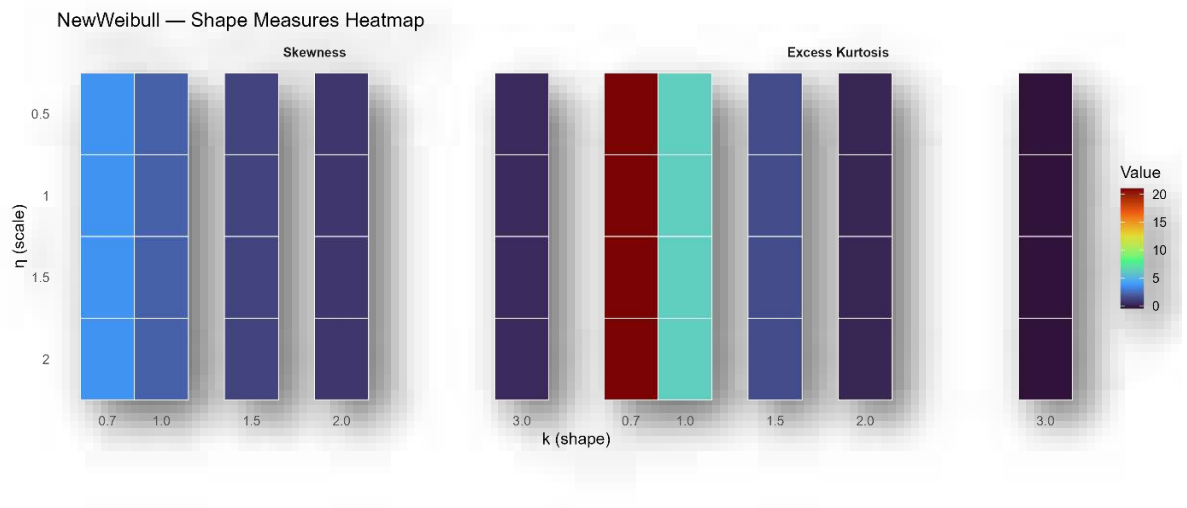

Figure 3. Shape Measures Heatmap.

To evaluate the temporal adaptability of the proposed NewWeibull distribution based trigonometric model, Figure 4 presents the PDF and HRF under three representative parameter configurations, each capturing a qualitatively distinct time-to-event profile. The red curve (η = 1.1, k = 2.1) exhibits a sharply peaked PDF concentrated near the origin, indicative of early event clustering. Its corresponding HRF rises rapidly and monotonically, signifying a sharply increasing instantaneous risk—characteristic of acute systems, such as the initial phase of infectious outbreaks marked by rapid case acceleration.

In contrast, the green curve (η = 1.8, k = 1.2) reflects a broader PDF with a more gradual ascent and descent, suggesting greater temporal dispersion in event occurrences. The associated HRF reveals a non-monotonic pattern, exhibiting a brief early decline followed by a gradual and sustained increase. This structure is reflective of dynamic systems wherein initial stabilization—perhaps due to containment or interventions followed by a delayed resurgence in risk, a scenario commonly observed during intermediate stages of epidemics or post-suppression rebounds.

The blue curve (η = 3.9, k = 3.4) is defined by a right-skewed PDF with a delayed peak, representing late-onset behavior. Its HRF increases steadily in a near-linear fashion, capturing cumulative hazard accumulation over time—typical of degradation-prone systems, latency-driven phenomena, or environments in which exposure risk escalates gradually.

Collectively, these parameterizations highlight the model's versatility in capturing early, transitional, and progressive hazard structures. This reinforces its applicability in real-world time-to-event modeling, including survival analysis, reliability studies, and temporally structured epidemiological forecasting, particularly where classical distributions may fall short in expressing complex or evolving risk dynamics.

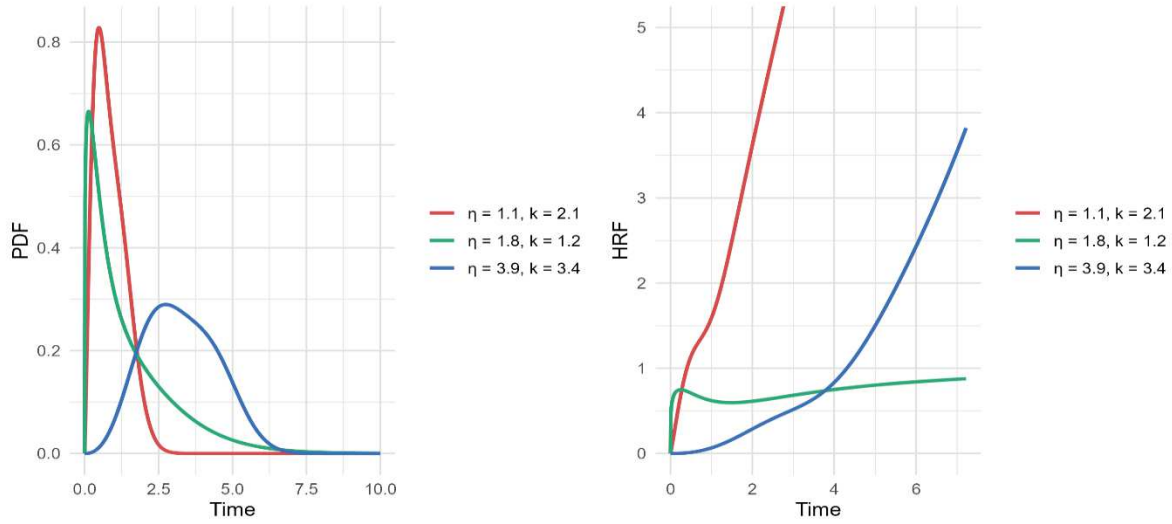

Figure 4. Density (left side) and Hazard Rate (right side) Functions Plots.

3.6. Shannon Entropy

For a continuous r.v. X with density $f_{X|(x;\eta,k)}$, the Shannon entropy is defined as:

$$\mathcal{H}_{X|(x;\eta,k)} = -\int_0^{\infty} f_{X|(\eta,k)}\, ln f_{X|(\eta,k)}\, dx. \tag{36}$$

For a T-G generated family, the CDF and PDF can be written as $F = H\big(G(x)\big)$ and $f = g(x)H'\big(G(x)\big)$, where $G(x)$ and $g(x)$ denotes the baseline CDF and PDF, respectively, and $H$is a monotone generator. Substituting this representation into Equation (36), we get

$$\mathcal{H}_{X|(x;\eta,k)} = -\int_0^{\infty} g(x;\theta)\; H'\big(G(x;\theta)\big)\big[ln\, g(x;\theta) + \; ln\, H'\left(G(x;\theta)\right)\big]dx. \tag{37}$$

For NewWeibull distribution substitution,

Let

$$t = \left(\frac{x}{\eta}\right)^k,$$

$$dt = \frac{k}{\eta}\left(\frac{x}{\eta}\right)^{k-1} dx,$$

which implies

$$g(x;\eta,k)\, dx = e^{-t}\, dt, \qquad ln\, g(x;\eta,k) = ln\left(\frac{k}{\eta}\right) + \frac{k-1}{k} ln\, t - t.$$

Moreover, $G(x;\eta,k)\, dx = 1 - e^{-t}$. Substituting into Equation (37) gives

$$\mathcal{H}_{X|(x;\eta,k)} = -\int_0^{\infty} e^{-t}\; H'(1-e^{-t}) \left[\; ln\left(\frac{k}{\eta}\right) + \frac{k-1}{k} ln\, t - t \; + \; ln\, H'\,(1-e^{-t})\right] dt\,.$$

Let's define

$$I_0 = \int_0^{\infty} e^{-t}\; H'(1-e^{-t})\, dt,$$

$$I_1 = \int_0^{\infty} e^{-t}\; H'(1-e^{-t})\; ln\, t\, dt,$$

$$I_2 = \int_0^{\infty} e^{-t}\; H'(1-e^{-t})\, t\, dt,$$

$$I_3 = \int_0^{\infty} e^{-t}\; H'(1-e^{-t})\; ln\, H'\,(1-e^{-t})\, dt.$$

Then

$$\mathcal{H}_{X|(x;\eta,k)} = -\ln\left(\frac{k}{\eta}\right) I_0 - \frac{k-1}{k} I_1 + I_2 - I_3. \tag{38}$$

One can get the closed forms for $I_0$and I_2; series for I_1. Using Equations (31)– (32):

$$I_0 = \int_0^1 H'(u)\, du = H(1) - H(0) = 1 = \sum_{m\geq 1} \frac{c_m}{m},$$

Using $\int_0^\infty te^{-\alpha t} tdt = \alpha^{-2}$,

$$I_2 = \sum_{m\geq 1} c_m \sum_{j=0}^{m-1} \frac{(-1)^j \binom{m-1}{j}}{(1+j)^2}. \tag{39}$$

Using $\int_0^\infty e^{-\alpha t} lntdt = \frac{-\gamma - ln\alpha}{\alpha}, \alpha > 0,$

where γ is Euler's constant, we get

$$I_1 = \sum_{m=1}^{\infty} c_m \sum_{j=0}^{m-1} (-1)^j \binom{m-1}{j} \frac{-\gamma - \ln(1+j)}{1+j}. \tag{40}$$

For series representation of I_3

$$H'(u) = c_1[1 + Z(u)],$$

$$Z(u) = \sum_{m=2}^{\infty} \frac{c_m}{c_1} u^{m-1}.$$

Since the series is convergent on [0,1), the logarithmic expansion

$$\ln H'(u) = \ln c_1 + \sum_{q=1}^{\infty} \frac{(-1)^{q+1}}{q} Z(u)^q,$$

is valid. Substituting $u = 1 - e^{-t}$ and applying dominated convergence gives

$$I_3 = ln(c_1)\, I_0 + \sum_{q=1}^{\infty} \frac{(-1)^{q+1}}{q} \int_0^\infty e^{-t}\, H'(1-e^{-t})\, Z(1-e^{-t})^q\, dt, \tag{41}$$

where each inner integral reduces to finite nested sums via Equation (32). Using $I_0 = 1$, Equation (38) simplifies to

$$\mathcal{H}_{X|(x;\eta,k)} = -\ln\left(\frac{k}{\eta}\right) - \frac{k-1}{k} I_1 + I_2 - I_3,$$

where I_1, I_2, and $I_3$are given by Equations (40), (39), and (41), respectively.

Table 3 shows a clear monotonic increase in Shannon entropy with the scale parameter η for every fixed shape k. For example, at $k = 0.7$, entropy rises from 0.1195 ($\eta = 0.5$) to 1.5058 ($\eta = 2$), while at $k = 3$ it increases from -0.3478 to 1.0385 over the same η range. Conversely, for a fixed η, entropy decreases as k increases, indicating reduced uncertainty with heavier shape control; at $\eta = 1$, entropy drops from 0.8126 ($k = 0.7$) to 0.3453 ($k = 3$). The heatmap in Figure 5 visually reinforces these numerical patterns: warmer colors concentrate at higher η and lower k, while cooler tones appear for larger k and smaller η. Finally, maximum uncertainty is attained for small k and large η (For instance, $k = 1, \eta = 2$ with entropy 1.5357), whereas negative or near-zero entropy values at low η and high k (For instance, $k = 3, \eta = 0.5$) reflect highly concentrated distributions.

Table 3. Shannon entropy metrics with parameter combinations (k, η).

k	η	Shannon entropy
0.7	0.5	0.119492854
	1	0.812640034
	1.5	1.218105143
	2	1.505787215

1	0.5	0.149415316
	1	0.842562497
	1.5	1.248027605
	2	1.535709678
1.5	0.5	0.04463708
	1	0.737784261
	1.5	1.143249369
	2	1.430931441
2	0.5	-0.092701557
	1	0.600445624
	1.5	1.005910732
	2	1.293592805
3	0.5	-0.347823229
	1	0.345323952
	1.5	0.75078906
	2	1.038471132

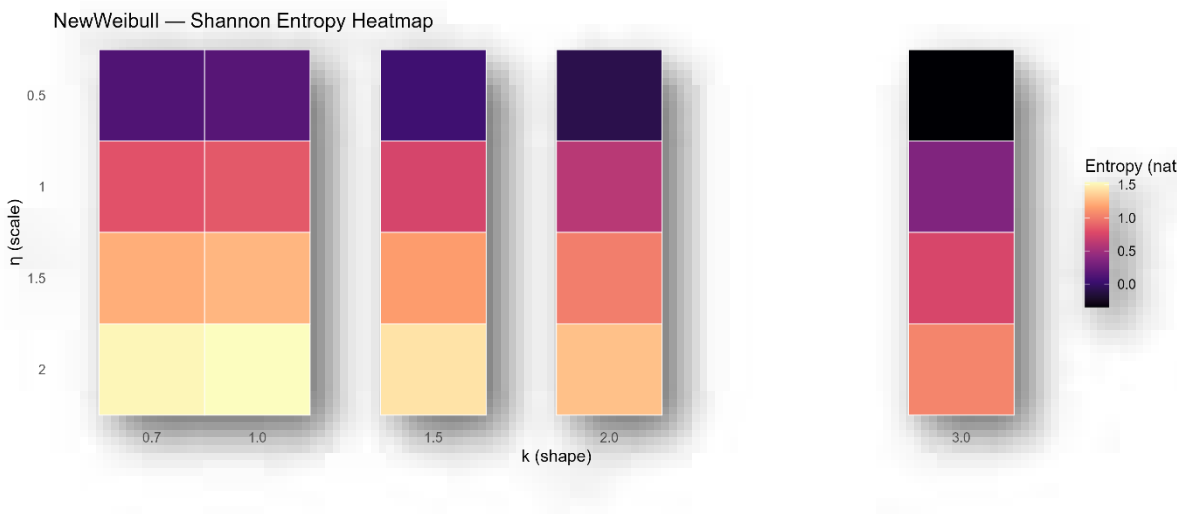

Figure 5. Shannon Entropy Heatmap.

3.7. Order Statistics

Let $x_1, \ldots, x_n \sim$ NewWeibull(η, k) with CDF $F_{X|(\eta,k)}$ and PDF $f_{X|(\eta,k)}$ on $x > 0$. Denote the r-th order statistic (OS) by $X_{r:n}(1 \leq r \leq n)$.

With reference to Equations (13a) and (14a) and Equations (19) and (20), the OS CDF $F_{X_{r:n}|(\eta,k)}$ and PDF $f_{X_{r:n}|(\eta,k)}$for the NewWeibull distribution of for $x > 0$ are

$$F_{X_{r:n}|(\eta,k)} = \sum_{j=r}^{n} \binom{n}{j} \left[\left[\frac{2\left\{1 - e^{-\left(\frac{x_j}{\eta}\right)^k}\right\}}{1 + sin\left\{\frac{\pi}{2}\left(1 - e^{-\left(\frac{x_j}{\eta}\right)^k}\right)\right\}} \right]^j \left[\frac{1 + sin\left[\frac{\pi}{2}\left\{1 - e^{-\left(\frac{x_j}{\eta}\right)^k}\right\}\right] - 2\left\{1 - e^{-\left(\frac{x_j}{\eta}\right)^k}\right\}}{1 + sin\left[\frac{\pi}{2}\left\{1 - e^{-\left(\frac{x_j}{\eta}\right)^k}\right\}\right]} \right]^{n-j} \right],$$

$$f_{X_{r:n}|(\eta,k)} = \left[\frac{n!}{(r-1)!\,(n-r)!} \left[\frac{2\left\{1 - e^{-\left(\frac{x_j}{\eta}\right)^k}\right\}}{1 + sin\left[\frac{\pi}{2}\left\{1 - e^{-\left(\frac{x_j}{\eta}\right)^k}\right\}\right]} \right]^{r-1} \times \left[\frac{1 + sin\left[\frac{\pi}{2}\left\{1 - e^{-\left(\frac{x_j}{\eta}\right)^k}\right\}\right] - 2\left\{1 - e^{-\left(\frac{x_j}{\eta}\right)^k}\right\}}{1 + sin\left[\frac{\pi}{2}\left\{1 - e^{-\left(\frac{x_j}{\eta}\right)^k}\right\}\right]} \right]^{n-r} \times \left[2\,\frac{k}{\eta}\left(\frac{x_j}{\eta}\right)^{k-1} e^{-\left(\frac{x_j}{\eta}\right)^k} \times \frac{\left[1 + sin\left[\frac{\pi}{2}\left\{1 - e^{-\left(\frac{x_j}{\eta}\right)^k}\right\}\right] - \left[\frac{\pi}{2}\left\{1 - e^{-\left(\frac{x_j}{\eta}\right)^k}\right\} cos\left[\frac{\pi}{2}\left\{1 - e^{-\left(\frac{x_j}{\eta}\right)^k}\right\}\right]\right]}{\left[1 + sin\left(\frac{\pi}{2}\left\{1 - e^{-\left(\frac{x_j}{\eta}\right)^k}\right\}\right)\right]^2} \right] \right]$$

3.8. Residual Function

Let X be a non-negative *r.v.* with survival function. For a fixed age $M > 0$, the residual life function is defined as

$$R_M(n) = Pr(\,X - M > n \mid X > M\,), \quad n \geq 0,$$

which simplifies

$$R_M(n) = \frac{S(M+n)}{S(M)}, \quad S(M) > 0. \tag{42}$$

Substitute Equations (23), into Equation (42) yields the explicit form as:

$$R_M(n;\eta,k)=\left[\frac{1+sin\left(\frac{\pi}{2}\left[1-e^{-\left((M+n)/\eta\right)^k}\right]\right)-2\left[1-e^{-\left((M+n)/\eta\right)^k}\right]}{1+sin\left(\frac{\pi}{2}\left[1-e^{-\left((M+n)/\eta\right)^k}\right]\right)}\right]\times\left[\frac{1+sin\left(\frac{\pi}{2}\left[1-e^{-(M/\eta)^k}\right]\right)}{1+sin\left(\frac{\pi}{2}\left[1-e^{-(M/\eta)^k}\right]\right)-2\left[1-e^{-(M/\eta)^k}\right]}\right].$$

Similarly for a fixed threshold $M>0$, the reversed residual life function is defined as:

$$\bar{R}_M(n)=\Pr(M-X>n\mid X\le M),\quad 0\le n\le M,$$

which reduces to

$$\bar{R}_M(n)=\frac{F(M-n)}{F(M)},\quad F(M)>0. \tag{43}$$

Hence the reversed residual life function is obtained by substituting the Equations (23), into Equation (43) that yields the explicit form as:

$$\bar{R}_M(n;\eta,k)=\left[\frac{2\left[1-e^{-\left((M-n)/\eta\right)^k}\right]}{1+sin\left(\frac{\pi}{2}\left[1-e^{-\left((M-n)/\eta\right)^k}\right]\right)}\right]\times\left[\frac{1+sin\left(\frac{\pi}{2}\left[1-e^{-(M/\eta)^k}\right]\right)}{2\left[1-e^{-(M/\eta)^k}\right]}\right].$$

Let the survival function be $S_{t|(\eta,k)}=1-F_{t|(\eta,k)}$. The mean residual life (MRL) is given by

$$\mathrm{MRL}(t)=\mathbb{E}[X-t|_{X>t}]=\frac{1}{S_{t|(\eta,k)}}\int_t^{\infty}S_{u|(\eta,k)}\,du.$$

Using the tail moment identity $\int_t^{\infty}S_{u|(\eta,k)}\,du=\mathbb{E}[X-t|_+]$ and $\mathbb{E}[X-t|_+]=\bar{m}_1(t)-tS_{t|(\eta,k)}$, we obtain the computational form

$$\mathrm{MRL}(t)=\frac{\bar{m}_1(t)}{S_{t|(\eta,k)}}-t=\frac{\mu_1-m_1(t)}{S_{t|(\eta,k)}}-t,$$

where $m_1(t)$ is 1st incomplete moment (reference to Equation (35*d*)).

The reversed mean residual life (RMRL) function is defined as

$$\mathrm{RMRL}(t)=\mathbb{E}(t-X|_{X\le t}).$$

Using the definition of conditional expectation,

$$\mathrm{RMRL}(t)=t-\frac{1}{F_{t|(\eta,k)}}\int_0^t x\,f_{X|(\eta,k)}dx=t-\frac{m_1(t)}{F_{t(\eta,k)}},$$

where $m_1(t)$ is the first incomplete moment (reference to Equation (35*d*)).

3.9. Inequality Curve

For $p\in(0,1)$, define the quantile q_p implicitly by

$$F_X(q_p)=p.$$

The Lorenz curve (LC) is defined by

$$LC(p)=\frac{1}{\mu}\int_0^{q_p}x\,f_{X|(\eta,k)}dx=\frac{m_1(q_p)}{\mu},$$

The Bonferroni curve is defined as

$$B(p)=\frac{1}{p\mu}\int_0^{q_p}x\,f_{X|(\eta,k)}dx=\frac{m_1(q_p)}{p\mu}.$$

The Generalized Lorenz Curve (GLC) is given by

$$GLC(p)=\int_0^{q_p}x\,f_{X|(\eta,k)}dx=m_1(q_p),$$

which combines inequality and scale effects and satisfies

$$GL(p)=\mu L(p).$$

The Zenga curve (ZC) is defined as

$$ZC(p) = 1 - \frac{\mu^{-}(p)}{\mu^{+}(p)} = 1 - \frac{(1-p)m_1(q_p)}{p\left(\mu - m_1(q_p)\right)},$$

where

$$\mu^{-}(p) = \frac{1}{p}\int_0^{q_p} x\, f_{X|(\eta,k)}dx = \frac{m_1(q_p)}{p},$$

$$\mu^{+}(p) = \frac{1}{1-p}\int_{q_p}^{\infty} x\, f_{X|(\eta,k)}dx = \frac{\mu - m_1(q_p)}{1-p}.$$

The Atkinson Inequality Curve (AIC) for inequality aversion parameter $\varepsilon > 0$, $\varepsilon \neq 1$ is defined as

$$AIC_{\varepsilon}(p) = 1 - \frac{1}{\mu}\left[\frac{1}{p}\int_0^{q_p} x^{1-\varepsilon} f_{X|(\eta,k)}dx\right]^{\frac{1}{1-\varepsilon}},$$

$$AIC_{\varepsilon}(p) = 1 - \frac{1}{\mu}\left[\frac{m_{1-\varepsilon}(q_p)}{p}\right]^{\frac{1}{1-\varepsilon}},$$

where $m_{1-\varepsilon}(\cdot)$ denotes the $(1-\varepsilon)$ −th incomplete moment.

Figures 6–7 show that inequality behavior is strongly parameter-dependent, with higher-intensity configurations producing a LC farther from the equality line, a sharper decline in the BC, steeper GLC growth, deeper ZC disparities, and larger AIC inequality, indicating strong concentration within smaller population shares. In contrast, lower-intensity parameter settings keep all curves closer to their respective equality benchmarks, reflecting a more homogeneous distribution. These patterns are consistently confirmed by the heatmaps across fixed percentiles ($p = 0.25, 0.5, 0.75, 0.9$), where warmer regions correspond to higher inequality under intense parameter settings and cooler regions indicate reduced inequality under milder configurations.

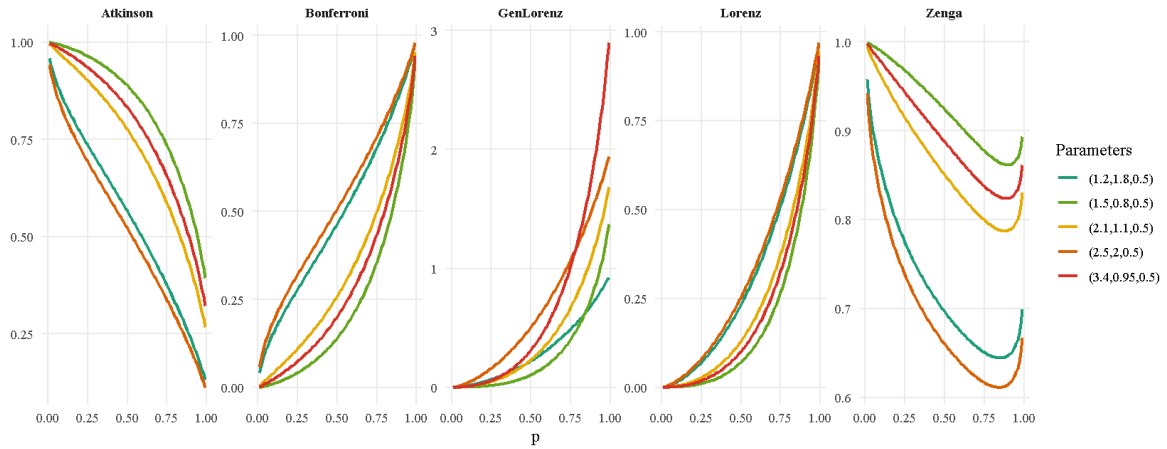

Figure 6. Inequality Curves Line Chart.



Figure 7. Inequality Curves Heatmap.

3.10. Risk measure

For a confidence level $p \in (0,1)$, define q_p as the unique solution of

$$F(q_p) = p.$$

The Value-at-Risk at level p is defined by

$$(VaR)_p = q_p.$$

The Tail Value-at-Risk (Conditional Tail Expectation) is

$$\text{TVaR}p = E[\,X \mid X > \text{VaR}p\,] = \frac{1}{1-p}\int_{q_p}^{\infty} x f_{X|(\eta,k)}dx.$$

The conditional tail variance is

$$\text{TailVar}_{\text{p}} = \text{Var}(\,X \mid X > q_p\,) = \frac{\mu_2 - m_2(q_p)}{1-p} - \left(\frac{\mu - m_1(q_p)}{1-p}\right)^2,$$

where $m_1(\cdot)$ and $m_2(\cdot)$ are 1st and 2nd incomplete moments (reference to Equations (35*d*) and (35*e*)).

Figure 8 shows a clear monotonic increase in all risk measures (VaR, TVaR, and TailVar) as the confidence level p increases, confirming growing tail risk at higher probability levels. For each fixed shape parameter k, larger values of the scale parameter a consistently produce higher risk levels, indicating stronger tail heaviness. The effect is most pronounced for smaller k (e.g., $k = 0.5$), where TailVar and TVaR rise sharply, whereas for larger k the curves remain comparatively flatter, reflecting lighter tails. The figure highlights the joint sensitivity of tail risk to both p and the parameter combination (a, k).

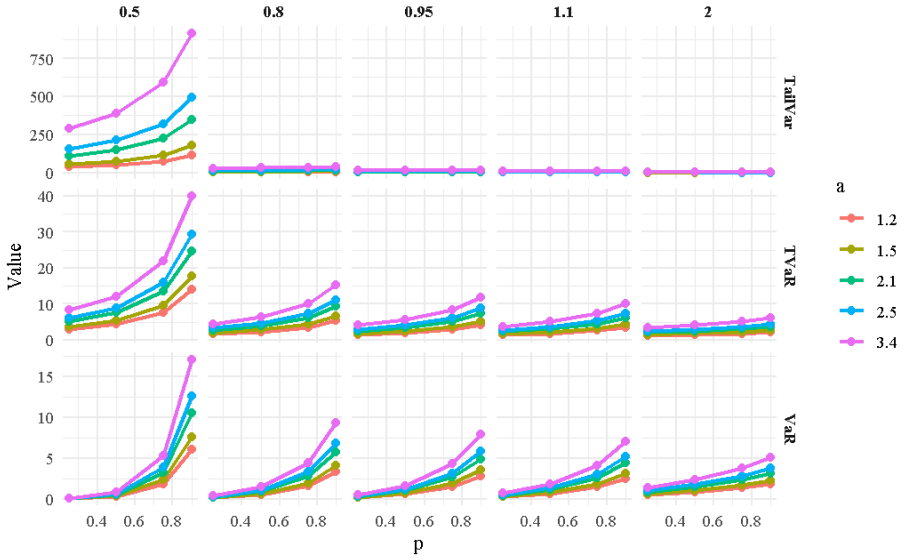

Figure 8. Risk Measures Plot.

3.11.Inference

Let $x_1, \ldots, x_n$ be i.i.d. from the NewWeibull distribution with (η, k). With the T–G family of distributions construction $F_{X|(x;\eta,k)} = H\big(G(x;\eta,k)\big)$, the density factors as:

$$f_{X|(x;\eta,k)} = g(x;\eta,k)\, H'\big(G(x;\eta,k)\big),$$

where, for the Weibull baseline,

$$t(x) = \left(\frac{x}{\eta}\right)^k, \quad G(x;\eta,k) = 1 - e^{-t(x)}, \quad g(x;\eta,k) = \frac{k}{\eta}\left(\frac{x}{\eta}\right)^{k-1} e^{-tx}.$$

Hence the log-likelihood function is presented as:

$$\ell(\eta,k) = \sum_{i=1}^{n} ln\, f_X\,(x_i;\eta,k) = \sum_{i=1}^{n} \{\, ln\, g\,(x_i;\eta,k) + ln\, H'\,\big(G(x_i;\eta,k)\big)\}.$$

Write, for each i,

$$t_i = \left(\frac{x_i}{\eta}\right)^k, \quad G_i = 1 - e^{-t_i}, \quad B_i = ln\left(\frac{x_i}{\eta}\right).$$

The partial derivative of t_i and G_i w.r.t η and k:

$$\frac{\partial t_i}{\partial \eta} = -\frac{k}{\eta}\, t_i, \qquad \frac{\partial t_i}{\partial k} = t_i\, B_i,$$

$$\frac{\partial G_i}{\partial \eta} = e^{-t_i}\frac{\partial t_i}{\partial \eta} = -\frac{k}{\eta}\, t_i(1 - G_i),$$

$$\frac{\partial G_i}{\partial k} = e^{-t_i}\frac{\partial t_i}{\partial k} = (1 - G_i)\, t_i B_i.$$

For the Weibull density part,

$$\frac{\partial}{\partial \eta} ln\, g\,(x_i) = \frac{k}{\eta}(t_i - 1), \qquad \frac{\partial}{\partial k} ln\, g\,(x_i) = \frac{1}{k} + B_i(1 - t_i).$$

Link derivative. For the trigonometric link

$$H(u) = \frac{2u}{1 + sin\left(\frac{\pi}{2}u\right)}, \qquad H'(u)\frac{2\left[1 + sin\left(\frac{\pi}{2}u\right) - \frac{\pi}{2}ucos\left(\frac{\pi}{2}u\right)\right]}{\left[1 + sin\left(\frac{\pi}{2}u\right)\right]^2},$$

define

$$D_G(u) = \frac{d}{du} \ln H'(u) = \frac{H''(u)}{H'(u)}.$$

A suitable closed form (with $\alpha = \pi/2$) is presented as:

$$D_G(u) = \frac{\alpha^2 u \ sin(\alpha u)}{1 + sin(\alpha u) - \alpha u \, cos(\alpha u)} - \frac{2\alpha \, cos(\alpha u)}{1 + sin(\alpha u)},$$

$$\text{i.e.} \quad D_G(u) = \frac{\frac{\pi^2}{4} G sin\left(\frac{\pi}{2}u\right)}{\left(1 + sin\left(\frac{\pi}{2}u\right) - \frac{\pi u}{2} cos\left(\frac{\pi}{2}u\right)\right) - \left[\frac{\pi \, cos\left(\frac{\pi}{2}u\right)}{1 + sin\left(\frac{\pi}{2}u\right)}\right]}. \tag{44}$$

Score equations. Using the chain rule

$$\frac{\partial l}{\partial \eta} = \sum_{i=1}^{n} \left[\frac{k}{\eta}(t_i - 1) + D_G(G_i)\frac{\partial G_i}{\partial \eta}\right] = \sum_{i=1}^{n} \frac{k}{\eta}\left[t_i - 1 - t_i(1 - G_i)D_G(G_i)\right], \tag{45}$$

$$\frac{\partial l}{\partial k} = \sum_{i=1}^{n} \left[\frac{1}{k} + B_i(1 - t_i) + D_G(G_i)\,\frac{\partial G_i}{\partial k}\right] = \sum_{i=1}^{n} \left[\frac{1}{k} + B_i\{\,1 - t_i + D_G(G_i)(1 - G_i)t_i\,\}\right]. \tag{46}$$

Observed information (structure). Let $D'_G(G) = \frac{d}{dG} D_G(G)$ (closed form follows by differentiating Equation (44)). Then, $\theta_j, \theta_k \epsilon \{\eta, k\}$

$$\frac{\partial^2 l}{\partial \theta_j \partial \theta_k} = \sum_{i=1}^{n} \left[\frac{\partial^2}{\partial \theta_j \partial \theta_k} ln\, g\,(x_i; \eta, k) + D'_G(G_i)\, G_{i,\theta_j}\, G_{i,\theta_k} + D_G(G_i)\, G_{i,\theta_j \theta_k}\right],$$

Asymptotics. Under standard regularity and identifiability conditions, the MLE $\left(\hat{\eta}, \hat{k}\right)$ solves Equations (45)–(46) and is consistent and asymptotically normal:

$$\sqrt{n}\left(\left(\hat{\eta}, \hat{k}\right)^T - (\eta, k)^T\right) \underset{\rightarrow}{d} \mathcal{N}(0, I(\eta, k)^{-1}),$$

where $I(\eta, k)^{-1} = \frac{\partial^2 l}{\partial \theta \partial \theta^T}$is the Fisher Information Matrix.

4. Results

4.1. Geographic Overview

The five urban centers selected from the Aseer Region of Saudi Arabia—Ahad Rifaydah, Billasmar, Sarat Abidah, and Al Harajah—represent diverse geographic characteristics in terms of elevation, climate, and urban structure (Table 4). Billasmar and Sarat Abidah lie in elevated, mountainous zones with moderate to semi-arid climates, characterized by smaller, more dispersed populations. Ahad Rifaydah, situated along a regional transport corridor, exhibits a mixed urban–rural profile, while Al Harajah lies in a more isolated lowland area. Abha, the regional administrative hub located on a high-altitude plateau of the Sarawat range, combines a dense urban core with extensive services and intercity connectivity; its cooler temperatures, year-round mobility, and role as a health and commercial center imply larger contact networks than surrounding localities.

These geographic distinctions are relevant to understanding the spatial distribution and intensity of COVID-19 transmission, providing essential context for the moment-based and statistical analyses that follow.

Table 4. Geographic summary of selected cities of region Aseer (Saudi Arabia).

City	Observation Period	Latitude	Longitude	Total Cases	Duration (Days)
Ahad Rifaydah	May 31 – Sept 1, 2020	18.2033	42.8344	475	26
Billasmar	June 1, 2020 – Jan 21, 2022	19.0555	42.3091	661	53
Sarat Abidah	June 29 – July 25, 2020	18.0606	43.1702	589	45
Al Harajah	July 2 – Aug 15, 2020	17.9258	43.5034	332	25
Abha	May 7– June 30, 2021	18.2164	42.5053	393	17

Data source: https://datasource.kapsarc.org/pages/home/ (KAPSARC Data Portal) (See Appendix A.1).

4.2. Descriptive Analysis

In this section, distributional features of COVID-19 daily case counts are summarized using the five-number summary (min, Q_1, median, Q_3, max) together with the first five summary measures reported in Table 5 (μ_1 = mean, μ_2 = variance, μ_3= skewness, μ_4 = kurtosis).

Billasmar shows the strongest right-tail and peak: μ_3 = 2.818 and μ_4 = 14.169. Its maximum of 66 versus a median of 8 highlights infrequent but severe spikes, consistent with heavier tails despite a modest center.

Ahad Rifaydah is the most variable by dispersion: $\mu_2 = 257.485$ is the largest variance among cities. Counts range from $1-62$ (min $= 1$, max $= 62$), indicating substantial day-to-day fluctuation; skewness and kurtosis are moderate (μ_3 = 1.079, μ_4 = 3.334).

Sarat Abidah is also markedly skewed and leptokurtic ($\mu_3 = 2.453, \mu_4 = 10.507$). Its interquartile span is broad ($Q_1 = 3$ to $Q_3 = 16$; IQR $= 13$), and the maximum reaches 72, confirming episodic surges atop a relatively low median (8).

Al Harajah has the lowest central level and variability ($\mu_1 = 9.80$, $\mu_2 = 98.833$) with a compressed range ($min = 1, max = 35$). Skewness and kurtosis are modest ($\mu_3 = 1.215$, $\mu_4 = 3.525$), consistent with a steadier outbreak profile.

Abha presents the highest central tendency ($\mu_1 = 23.118$) with moderate dispersion ($\mu_2 = 179.860$), near-symmetry ($\mu_3 = 0.262$), and sub-Gaussian tails ($\mu_4 = 1.697 < 3$); together with a relatively high median (19) and IQR span $13 - 32$, this indicates persistently elevated daily counts with fewer extreme spikes (max = 45) compared with the other cities.

Overall, variance is highest in Ahad Rifaydah, whereas tail heaviness and asymmetry are most pronounced in Billasmar. Sarat Abidah combines moderate dispersion with heavy right tails, and Al Harajah is comparatively stable.

Table 5. Summary statistics for selected cities of region Aseer (Saudi Arabia).

Statistic	Ahad Rifaydah	Billasmar	Sarat Abidah	Al Harajah	Abha
μ_1	18.26923077	10.80769231	12.44444444	9.80000000	23.11764706
μ_2	257.4846154	117.8054299	177.479798	98.83333333	179.8602941
μ_3	1.078817122	2.817979181	2.45287837	1.215176601	0.262013346
μ_4	3.33388219	14.16927558	10.50694467	3.524842954	1.696759584
Min	1	1	1	1	4
Q_1	6	4	3	2	13
Median	12	8	8	7	19
Q_3	29	15	16	17	32
Max	62	66	72	35	45

4.3. Epidemiological Analysis

In this section, we evaluate the probabilistic behavior of COVID-19 daily case distributions across selected urban centers in the Aseer Region using a suite of competing parametric models. The candidates include classical Weibull, Gamma, LogNormal, Exponential, Exponentiated Exponential [], and Sin Weibull by Faruk et al. [33], distributions, alongside the proposed NewWeibull distribution. Model performance is assessed with three complementary criteria: the Kolmogorov–Smirnov (KS) statistic and its p-value for global agreement; the Anderson–Darling Estimate (ADE) for tail sensitivity; and the Cramér–von Mises Estimate (CVME) for cumulative deviations. The best fit is defined by the lowest ADE and CVME combined with a non-significant KS (i.e., high p-value). Graphical diagnostics (PDFs, CDFs, and Q–Q plots) provide an additional visual check.

For Ahad Rifaydah (Table 6; Figure 9), the NewWeibull distribution clearly dominates: it attains the lowest CVME (0.028) and the highest KS p-value (0.989), while maintaining the smallest ADE (0.189). In contrast, the Sin Weibull distribution exhibits heavy overfitting (ADE > 4.59) and a near-zero KS p-value, confirming poor generalization despite extra flexibility.

For Billasmar (Table 7; Figure 10), where the surveillance window is long and the empirical distribution is notably volatile, the NewWeibull distribution again performs best across the joint criteria, delivering the most balanced KS–ADE–CVME profile amid pronounced right-tail behavior. Classical baselines (Weibull/Gamma/LogNormal) are competitive distributions but consistently lag on CVME and tail fit.

For Sarat Abidah (Table 8; Figure 11), characterized by episodic surges, the NewWeibull distribution maintains stability with ADE = 0.500 and CVME = 0.068, edging out alternatives that either lose tail fidelity (higher ADE) or inflate global error (higher CVME). This result underscores the model's resilience to short, bursty outbreaks.

For Al Harajah (Table 9; Figure 13), the NewWeibull distribution again yields the most balanced trade-off, with CVME = 0.067 and a respectable KS p-value (0.791), outperforming the classical Weibull and Gamma distributions on both global and tail metrics in a relatively short, skewed series.

For Abha (Table 10; Figure 12), which represents a concentrated urban transmission profile, the New Weibull distribution provides the best overall fit with CVME = 0.04349 and ADE = 0.28933, paired with a KS p-value of 0.9711. The nearest competitor on CVME is the Exponentiated Exponential distribution (CVME = 0.04561), which the NewWeibull distribution improves upon by ≈ 4.7%; on tail sensitivity, it improves over the same competitor's ADE = 0.30808 by ≈6.1%.

Other baselines rank further behind: Gamma (CVME = 0.04740; ADE = 0.31447), LogNormal (0.05199; 0.36776), and Weibull (0.05249; 0.33113). The plain Exponential distribution performs poorly (CVME = 0.21591; ADE = 1.28285), and Sin Weibull again collapses (CVME = 0.84525; ADE = 3.90508). Parameter estimates for Abha, $\hat{\eta} = 28.309$ (SE 3.358) and $\hat{k} = 2.2455$ (SE 0.3977), align with a moderately right tailed but well-behaved hazard structure, consistent with an urban center exhibiting concentrated bursts rather than extremely heavy tails.

These city-level results show the NewWeibull distribution to be both statistically superior and practically adaptable across heterogeneous outbreak regimes—from concentrated urban transmission (Abha) to long-tailed, lower-density volatility (Billasmar), and from short, surge-prone episodes (Sarat Abidah) to brief, skewed series (Al Harajah). The consistent gains in CVME and ADE, alongside high KS p-values, argue for next-generation flexible models when classical symmetry or homogeneity assumptions fail to capture real-world epidemiological dynamics.

Table 6. Estimates and fit statistics for city Ahad Rifaydah, region Aseer, Saudi Arabia dataset.

Model	Estimates (Standard Error)		Fit Statistics			
	$\hat{\eta}$	$\hat{k}$	KS	(KS)P-Value	ADE	CVME
NewWeibull	22.785519 (3.693365)	1.384216 (0.195678)	0.086942491	0.989378682	0.188908476	0.028439424
Weibull	1.144503 (0.176655)	19.181205 (3.467004)	0.092346308	0.979596136	0.225047878	0.035330324
Gamma	1.246153 (0.310002)	0.068214 (0.020768)	0.094656481	0.973968792	0.216800447	0.032304028
Exponentiated Exponential	0.063190 (0.015264)	1.258802 (0.336252)	0.095083479	0.972826198	0.213409225	0.031276578
LogNormal	2.453016 (0.209272)	1.067082 (0.147977)	0.097584882	0.965467441	0.346221495	0.036137390
SinWeibull	4.969580 (0.821699)	0.460679 (0.064816)	0.344941997	0.00411107	4.595854128	0.929745019

Table 7. Estimates and fit statistics for city Billasmar, region Aseer, Saudi Arabia dataset.

Model	Estimates (Standard Error)		Fit Statistics			
	$\hat{\eta}$	$\hat{k}$	KS	(KS)P-Value	ADE	CVME
NewWeibull	13.632288 (1.696098)	1.342929 (0.123487)	0.076040641	0.924477313	0.490280385	0.053039256

Weibull	1.140552 (0.116230)	11.380372 (1.464723)	0.079962356	0.893648763	0.406427108	0.045399167
Gamma	1.360351 (0.241031)	0.125871 (0.026855)	0.09331004	0.755795691	0.379700763	0.051032973
LogNormal	1.969656 (0.131186)	0.946002 (0.092762)	0.091621776	0.775265777	0.451124318	0.069522322
Exponentiated Exponential	0.115642 (0.019481)	1.430197 (0.281741)	0.095673827	0.727953981	0.381499709	0.053455986
Exponential	0.092528 (0.012829)	*+*	0.111250349	0.540506102	0.720602556	0.082321843
SinWeibull	4.785041 (0.546788)	0.553827 (0.055644)	0.319949687	4.76E-05	8.771844581	1.74388299

Table 8. Estimates and fit statistics for city Sarat Abidah, region Aseer, Saudi Arabia dataset.

Model	Estimates (Standard Error)		Fit Statistics			
	$\hat{\eta}$	$\hat{k}$	KS	(KS)P-Value	ADE	CVME
NewWeibull	15.589330 (2.280445)	1.240917 (0.125579)	0.091818206	0.842505763	0.500373265	0.068370531
Weibull	1.051030 (0.116729)	12.71576 (1.909046)	0.092077923	0.840046486	0.407203723	0.051379475
LogNormal	2.035112 (0.154700)	1.037764 (0.109379)	0.105472001	0.698669974	0.492797177	0.080921036
Gamma	1.166887 (0.219480)	0.093771 (0.021871)	0.107581306	0.674911646	0.422832766	0.057287552
Exponentiated Exponential	0.090505 (0.017106)	1.203957 (0.246952)	0.111495612	0.63064382	0.429385405	0.058801348
SinWeibull	4.618315 (0.550943)	0.517271 (0.055816)	0.310990668	0.00033172	7.631024685	1.48954839

Table 9. Estimates and fit statistics for city Al Harajah, region Aseer, Saudi Arabia dataset.

Model	Estimates (Standard Error)		Fit Statistics			
	$\hat{\eta}$	$\hat{k}$	KS	(KS)P-Value	ADE	CVME
NewWeibull	11.854579 (2.238750)	1.199855 (0.167204)	0.130094442	0.791281341	0.463475474	0.067104285
Weibull	0.990502 (0.154471)	9.755375 (2.084005)	0.132723877	0.770623936	0.52303268	0.076301668
LogNormal	1.716325 (0.227407)	1.137039 (0.160783)	0.135903204	0.745008856	0.560062116	0.07992939
Exp	0.1020436 (0.020406)	*+*	0.136290213	0.741850844	0.541082089	0.079891398
Gamma	1.017998 (0.253898)	0.103880 (0.033090)	0.140186091	0.709685682	0.563338484	0.084103721
Exponentiated Exponential	0.103480 (0.027074)	1.021862 (0.269931)	0.140720989	0.70522588	0.566613142	0.084691999
SinWeibull	3.985980 (0.566637)	0.518789 (0.075107)	0.262506962	0.063775861	4.521971004	0.779231169

Table 10. Estimates and fit statistics for city Abha, region Aseer, Saudi Arabia dataset.

Model	Estimates (Standard Error)		Fit Statistics			
	$\hat{\eta}$	$\hat{k}$	KS	(KS)P-Value	ADE	CVME

NewWeibull	28.309105 (3.3583421)	2.245512 (0.3977067)	0.118358153	0.971103714	0.289325634	0.043487733
Exp	0.04325716 (0.01048579)	*+*	0.204831742	0.473647396	1.282851494	0.21590968
Gamma	2.6583567 (0.86054834)	0.1149939 (0.04096253)	0.129556662	0.937811778	0.314472008	0.047402047
LogNormal	2.9408630 (0.1654788)	0.6822865 (0.1170114)	0.13207914	0.92815936	0.367761521	0.05198628
Exponentiated Exponential	0.07728252 (0.01918936)	2.87650180 (1.10836333)	0.12908957	0.939512755	0.308084522	0.04560534
Weibull	1.851414 (0.3648109)	26.077046 (3.5984432)	0.120878394	0.964962872	0.331133845	0.052489762
SinWeibull	7.1429696 (2.00155440)	0.5099755 (0.09370144)	0.465834536	0.001249622	3.90507748	0.845246868

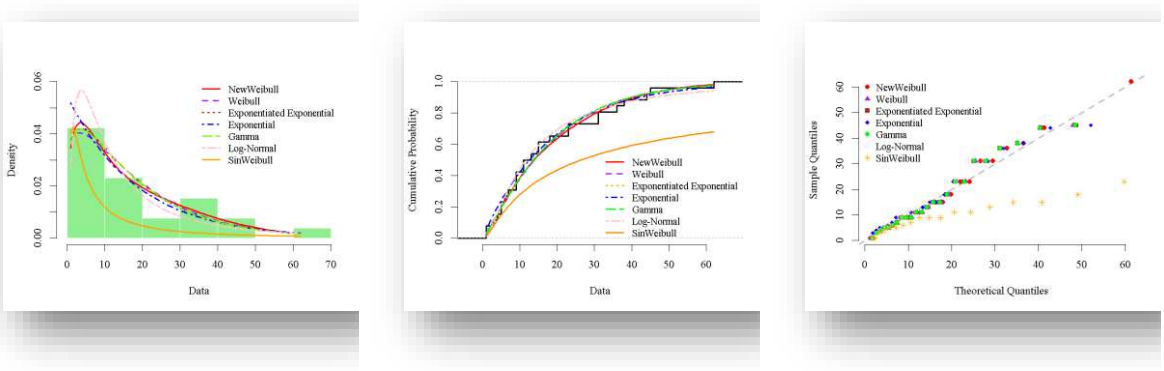

Figure 9. Fitted plots for Ahad Rifaydah, region Aseer, Saudi Arabia.

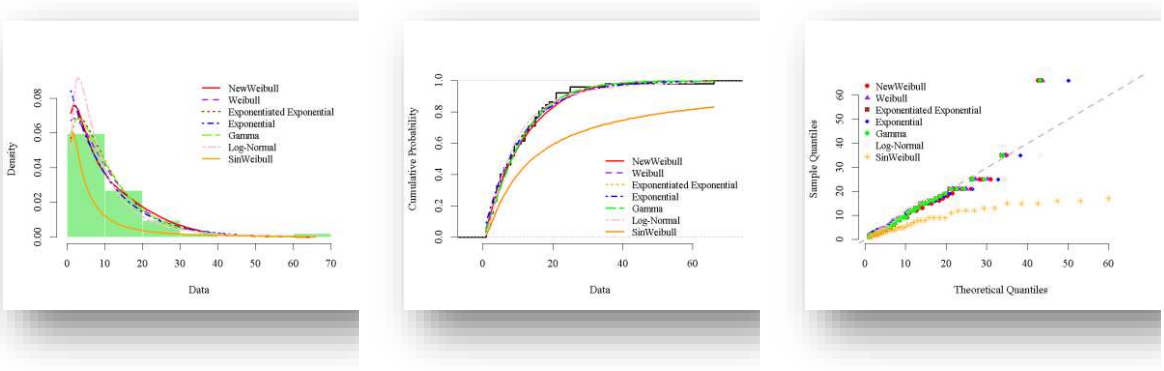

Figure 10. Fitted plots for Billasmar, region Aseer, Saudi Arabia.

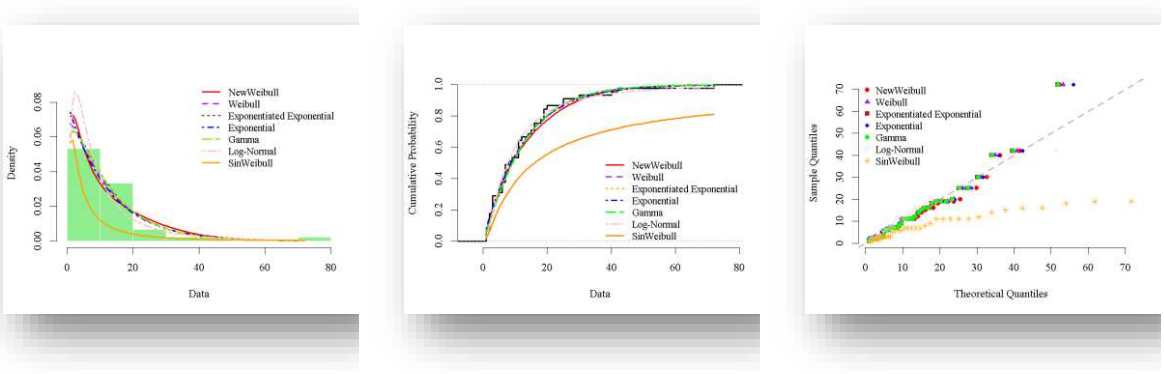

Figure 11. Fitted plots for Sarat Abidah, region Aseer, Saudi Arabia.

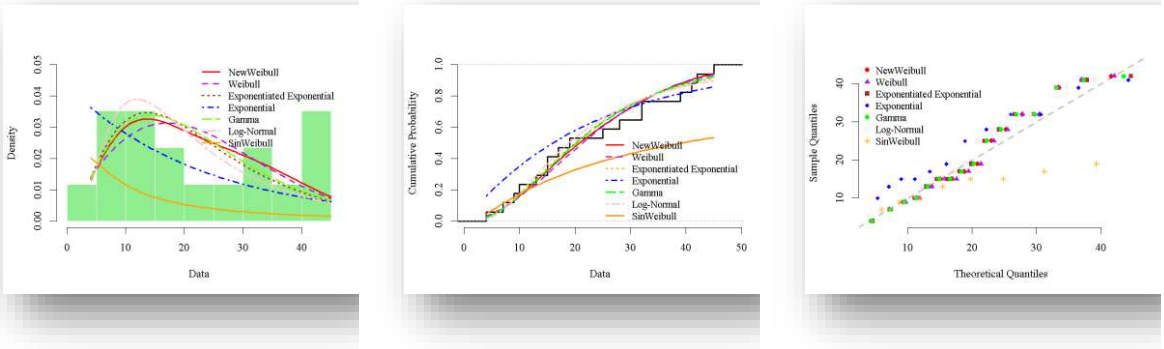

Figure 12. Fitted plots for Abha, region Aseer, Saudi Arabia.

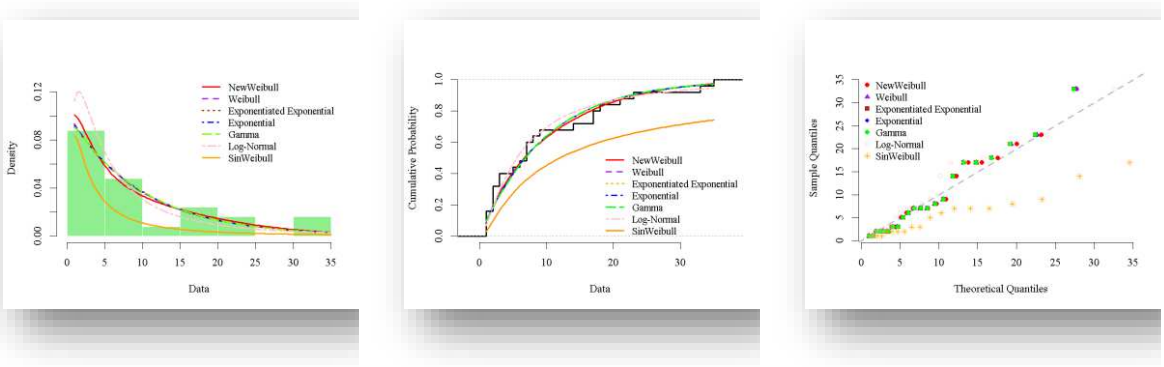

Figure 13. Fitted plot for Al Harajah, region Aseer, Saudi Arabia.

5. Simulation

In this section, the finite-sample performance of the maximum likelihood estimators $\hat{k}$ and $\hat{\eta}$ is examined through extensive simulations. For each parameter configuration, including representative combinations such as $(k = 0.7, \eta = 0.5)$, $(k = 1.0, \eta = 1.5)$, $(k = 1.5, \eta = 0.5)$, $(k = 2.0, \eta = 1.0)$, and $(k = 3.0, \eta = 2.0)$, random samples of size $n \in \{50,100,250,500,1000,2000\}$ were generated, and the procedure was repeated over $R = 500$ independent replications.

For an estimator $\hat{\theta}$ of a true parameter value θ\theta, we computed its:

- $\text{Mean}(\hat{\theta}) = 1/500 \sum_{r=1}^{500} \hat{\theta}_r$,
- standard deviation $\text{SD}(\hat{\theta}) = \sqrt{\frac{1}{499 \sum_{r=1}^{500} (\hat{\theta}_r - \overline{\hat{\theta}})^2}}$ with $\overline{\hat{\theta}} = \frac{1}{500 \sum_{r=1}^{500} \hat{\theta}_r}$,
- $\text{Bias}(\hat{\theta}) = \overline{\hat{\theta}} - \theta$, and

- Mean Squared Error: $\mathrm{MSE}(\hat{\theta}) = 1/500 \sum_{r=1}^{500} (\hat{\theta}_r - \theta)^2$.

The results, summarized in Tables 11–15 and illustrated in Figures 14-15, clearly demonstrate the asymptotic properties of the estimators: both $\hat{k}$ and $\hat{\eta}$ are consistent and approximately normal, with biases converging to zero, standard deviations shrinking at the expected $\mathcal{O}(1/\sqrt{n})$ rate, and mean squared errors decreasing monotonically as the sample size increases.

For small sample sizes, such as $n = 50$, the estimators display noticeable dispersion, with the standard deviations of $\hat{\eta}$ reaching as high as 0.264 (Table 12) and those of $\hat{k}$ ranging from 0.073 (Table 11) to 0.328 (Table 15). As the sample size grows, these variances decrease systematically, converging to values below 0.020 for $\hat{\eta}$ and below 0.050 for $\hat{k}$ when $n = 2000$. This trajectory is visible in Figures 14 and 15, where the SD panels reveal steep early declines followed by stabilization, in line with the theoretical $n^{-1/2}$ rate of convergence.

5.1. Mean Analysis

The mean values of the estimators also converge rapidly toward their true parameters. For instance, $\hat{\eta}$ at $(k, \eta) = (0.7,0.5)$shifts at 0.509 at $n = 50$ to 0.501 at $n = 2000$ (Table 11), while at $(k, \eta) = (1.0,1.5)$the mean tightens from 1.496 to 1.500 (Table 12). Similar convergence patterns are evident for $\hat{k}$: in the most challenging case with $k = 3.0$, the mean decreases from 3.095 at $n = 50$ to 2.998 at $n = 2000$ (Table 15). These shifts, illustrated in the mean panels of Figures 14 and 15, highlight the estimators' diminishing finite-sample bias as the sample size grows.

5.2. Bias Analysis

Bias values themselves provide further confirmation of consistency. For $\hat{\eta}$, bias magnitudes are generally below 0.01 even at $n = 50$, and they shrink to the order of 10^{-4} once $n \geq 1000$. For $\hat{k}$, initial small positive biases—such as 0.0946 at $k = 3.0, n = 50$ (Table 15)—steadily decrease and in some cases turn slightly negative, converging toward zero as expected under standard regularity conditions. These dynamics are depicted in the bias panels of Figures 14 and 15, where the trajectories flatten around the horizontal axis.

5.3. Mean Square Error Analysis

The MSEs combine these effects of variance and bias, showing consistent monotonic declines across all configurations. For $\hat{\eta}$ with $\eta = 1.5$, the MSE falls from 0.0697 at $n = 50$ to 0.0014 at $n = 2000$ (Table 12), while for $\hat{k}$ with $k = 3.0$, the MSE drops from 0.1163 to 0.0023 over the same range (Table 15). Figures 14 and 15 capture these trends, where the MSE curves demonstrate smooth convergence toward negligible levels as n grows.

The joint evidence from Tables 11–15 and Figures 14-15 confirms that both $\hat{k}$ and $\hat{\eta}$ exhibit the expected large-sample properties. With increasing sample size, their distributions concentrate tightly around the true parameter values, their biases vanish, and their variances diminish at the anticipated rate. By $n = 500$, the estimators already achieve sub-percent precision, while $n \geq 1000$ effectively place them in the asymptotic regime. These outcomes provide strong empirical support for the theoretical guarantees established in the asymptotic framework of the NewWeibull trigonometric model.

Across all designs, $\hat{\eta}$ is empirically easier to estimate than $\hat{k}$. At $n = 50$, the largest SD for $\hat{\eta}$ is 0.264 (Table 12) versus 0.328 for $\hat{k}$ (Table 15), and the worst absolute bias for $\hat{\eta}$ is only 0.0072 (Table 14) compared with 0.0946 for $\hat{k}$ (Table 15). By $n = 1000, \hat{\eta}$ has SD $0.013 - 0.055$ with biases typically 7×10^{-4}, whereas $\hat{k}$ still shows SD $(0.044 - 0.068)$ and small residual bias (e.g., $+0.0057$ at $k = 3.0$; Table 15). This gap is consistent with likelihood curvature: the scale-like η is tightly informed by the data range, while the shape k governs tail thickness and is intrinsically less identifiable at small n.

Practically, MSE for $\hat{k}$ remain wider at modest n, so two recommendations follow:

i. use stronger starting values or weakly informative prior/penalties for k (or reparametrize to $logk, log\eta$) to stabilize optimization; and

ii. target $n \geq 500$when precise inference on k is critical, as the simulations show both bias and variance for $\hat{k}$ settle into the asymptotic regime only beyond that point, while $\hat{\eta}$ is already near-unbiased and low-variance by $n \approx 250$.

Table 11. Simulated output for ($k = 0.7, \eta = 0.5$).

Est	n	Mean	SD	Bias	MSE
$\hat{k}$	50	0.72500054	0.07289434	0.02500054	0.00592799
	100	0.70695993	0.05129328	0.00695993	0.00267418
	250	0.70423491	0.03162099	0.00423491	0.00101582
	500	0.70242499	0.02421094	0.00242499	0.00059088
	1000	0.70040506	0.01561853	0.00040506	0.00024362
	2000	0.70074141	0.01161220	0.00074141	0.00013512
$\hat{\eta}$	50	0.50912771	0.12073735	0.00912771	0.01463167
	100	0.49942368	0.08133046	-0.00057633	0.00660175
	250	0.50231342	0.05269802	0.00231342	0.00277688
	500	0.50012839	0.03819355	0.00012839	0.00145585
	1000	0.50055212	0.02593350	0.00055212	0.00067151
	2000	0.50069998	0.01908543	0.00069998	0.00036402

Table 12. Simulated output for ($k = 1.0, \eta = 1.5$).

Est	n	Mean	SD	Bias	MSE
$\hat{k}$	50	1.01276932	0.10389500	0.01276932	0.01093564
	100	1.00999991	0.07210281	0.00999991	0.00528842
	250	1.00697135	0.04739913	0.00697135	0.00229078
	500	1.00072533	0.03334491	0.00072533	0.00111019
	1000	1.00123808	0.02280302	0.00123808	0.00052047
	2000	1.00024478	0.01647555	0.00024478	0.00027096
$\hat{\eta}$	50	1.49609674	0.26425288	-0.00390326	0.06970516
	100	1.50417072	0.16982203	0.00417072	0.02879924
	250	1.49311604	0.10791569	-0.00688396	0.01166989
	500	1.49937492	0.07365703	-0.00062509	0.00541490
	1000	1.50070013	0.05497060	0.00070013	0.00301621
	2000	1.50013726	0.03772848	0.00013726	0.00142061

Table 13. Simulated output for ($k = 1.5, \eta = 0.5$).

Est	n	Mean	SD	Bias	MSE
$\hat{k}$	50	1.53938868	0.16689572	0.03938868	0.02934994
	100	1.52063858	0.11590077	0.02063858	0.01383207
	250	1.50760762	0.06842764	0.00760762	0.00473085
	500	1.50352515	0.04696051	0.00352515	0.00221331
	1000	1.49886847	0.03312233	-0.00113153	0.00109618
	2000	1.50042721	0.02360791	0.00042721	0.00055640
$\hat{\eta}$	50	0.49666326	0.05247619	-0.00333674	0.00275938
	100	0.49773299	0.03693305	-0.00226701	0.00136646
	250	0.50009777	0.02422831	0.00009777	0.00058585
	500	0.49986679	0.01785296	-0.00013321	0.00031811
	1000	0.50008987	0.01217366	0.00008987	0.00014791

	2000	0.49964428	0.00877309	-0.00035572	0.00007694

Table 14. Simulated output for ($k = 2.0, \eta = 1.0$).

Est	n	Mean	SD	Bias	MSE
$\hat{k}$	50	2.04427314	0.20996406	0.04427314	0.04595685
	100	2.02732040	0.14767439	0.02732040	0.02251051
	250	2.01528825	0.09537572	0.01528825	0.00931207
	500	2.00603987	0.06388785	0.00603987	0.00410998
	1000	2.00539679	0.04430895	0.00539679	0.00198848
	2000	2.00155969	0.02913069	0.00155969	0.00084933
$\hat{\eta}$	50	0.99277950	0.07798262	-0.00722050	0.00612126
	100	0.99837249	0.05756262	-0.00162751	0.00330948
	250	1.00254624	0.03858016	0.00254624	0.00149194
	500	0.99808246	0.02787565	-0.00191754	0.00077917
	1000	0.99993542	0.01770390	-0.00006458	0.00031281
	2000	1.00040957	0.01328603	0.00040957	0.00017633

Table 15. Simulated output for ($k = 3.0, \eta = 2.0$).

Parameter	n	Mean	SD	Bias	MSE
$\hat{k}$	50	3.09459353	0.32801133	0.09459353	0.11632418
	100	3.04939623	0.22271027	0.04939623	0.05194065
	250	3.02293895	0.14315913	0.02293895	0.02097974
	500	3.01203376	0.09364095	0.01203376	0.00889590
	1000	3.00567681	0.06795533	0.00567681	0.00464092
	2000	2.99817396	0.04761080	-0.00182604	0.00226559
$\hat{\eta}$	50	1.99808833	0.11384550	-0.00191167	0.01293853
	100	1.99964214	0.08088089	-0.00035786	0.00652876
	250	2.00192274	0.05090470	0.00192274	0.00258980
	500	1.99916099	0.03609078	-0.00083901	0.00130064
	1000	1.99849188	0.02346791	-0.00150812	0.00055192
	2000	1.99940947	0.01793065	-0.00059053	0.00032121

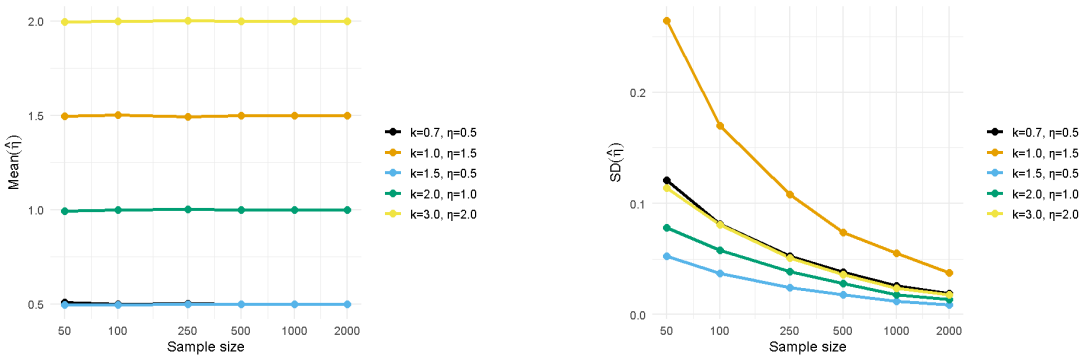

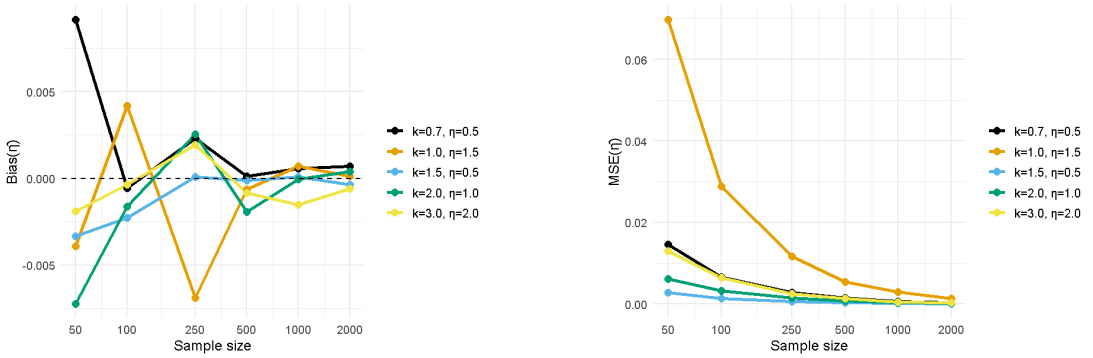

Figure 14. Simulated plots for $\hat{\eta}$.

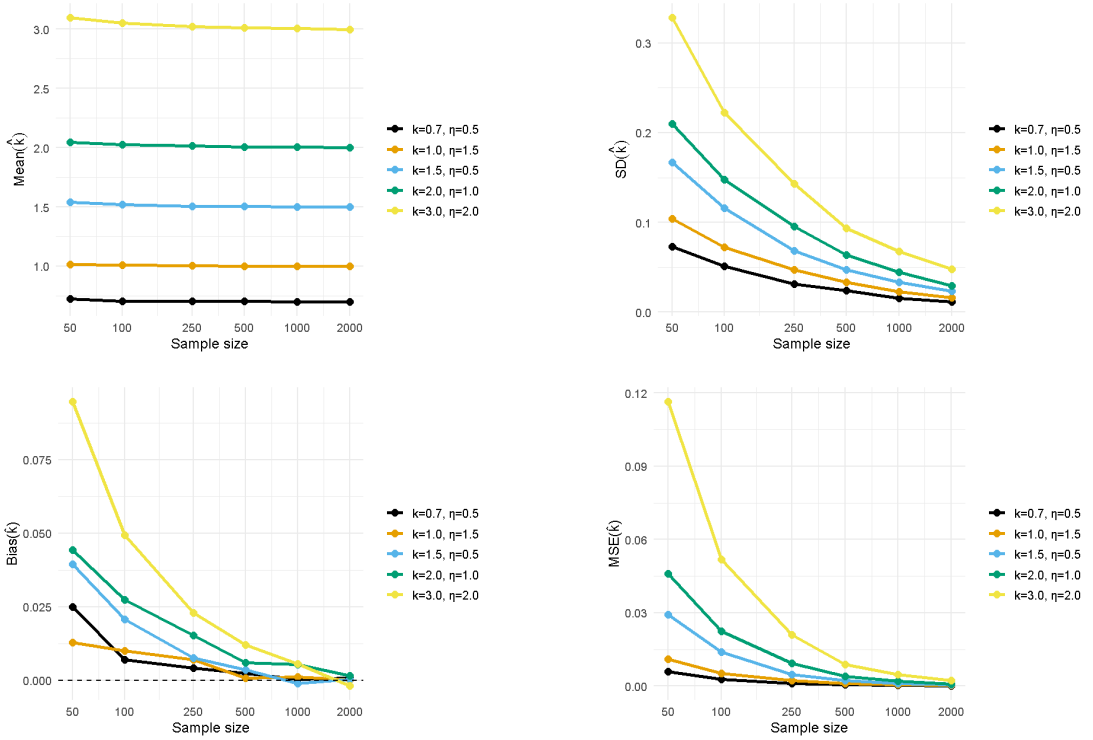

Figure 15. Simulated plots for $\hat{k}$.

6. Discussion

This paper advances both methodology and practice by unifying three strands of evidence—mathematical theory, controlled simulation, and city-level data analysis—to assess a new trigonometric-generated sub-model, the NewWeibull distribution. The theoretical results establish a clean moment representation via the Maclaurin expansion of $H'(u)$, conditions for the interchange of summation and integration, and the standard large-sample properties of the MLEs. The simulation study then stress-tests those properties across sample sizes $n \in \{50,100,250,500,1000,2000\}$, and the empirical section evaluates real COVID-19 daily case distributions from five urban centers in the Aseer region.

From a theoretical standpoint, the moment machinery shows that raw moments m_r decompose into weighted integrals, which are reducible to gamma-type forms under Weibull baselines model. This provides direct access to central moments, and shape measures and supports identifiability arguments. The asymptotic framework—regularity of the likelihood, existence and uniqueness of the maximizer, and Fisher information—predicts consistency and approximate normality for $(\hat{k}, \hat{\eta})$. These results are not merely formal; they predict the precise patterns later observed in the Monte Carlo study and the data fits.

The simulation evidence (Tables 11–15; Figures 14–15) aligns tightly with the theory. For $\hat{\eta}$, means are flat at the true value across all designs, SDs shrink at the expected rate, and biases are numerically negligible by $n \geq 1000$ (often $\leq 7 \times 10^{-4}$). For $\hat{k}$, finite-sample bias is slightly positive at small n (e.g., $k = 3.0$ shows bias 0.0946 at $n = 50$) but decays quickly, crossing zero near $n \approx 1000$. MSE declines monotonically for both parameters—for instance, with $\eta = 1.5$ it falls from 0.0697 to 0.00142, and with $k = 3.0$ from 0.1163 to 0.00227 as n moves from 50 to 2000. A practical implication is asymmetry in difficulty: η is easier to estimate than k at small to moderate n. Accordingly, inference that targets the shape k benefits from $n \geq 500$ and from optimization on the log-scale (or weak penalties) to stabilize small-sample curvature.

The empirical analysis confirms that these estimation properties translate into superior real-world fits. Across cities, the NewWeibull distribution consistently pairs low ADE and CVME with high KS p-values, outperforming classical Weibull, Gamma, LogNormal, Exponential, and the more flexible SinWeibull distributions. In Ahad Rifaydah (Table 6; Figure 9), NewWeibull distribution attains CVME 0.028 and KS p-value 0.989 with the smallest ADE (0.189), while Sin Weibull distribution exhibits severe overfitting (ADE $>$ 4.5; KS p $\approx$ 0.004). In Billasmar (Table 7; Figure 10), where tails are heaviest, NewWeibull distribution again leads to the joint criteria; the plain Exponential and SinWeibull distributions degrade markedly on CVME and ADE. Sarat Abidah (Table 8; Figure 11) shows episodic surges; NewWeibull distribution maintains tail control (ADE $\approx$ 0.500; CVME $\approx$ 0.068) with competitive KS. Al Harajah (Table 9; Figure 13) is shorter and more skewed; NewWeibull distribution yields the most balanced trade-off (CVME $\approx$ 0.067; KS p $\approx$ 0.79). Abha (Table 10; Figure 12) reflects concentrated urban transmission; NewWeibull distribution attains CVME 0.0435 and ADE 0.2893 with KS p-value 0.9711, improving upon the nearest competitor on both global and tail metrics.

Finally, the NewWeibull distribution contributes to a mathematically well-founded and empirically effective option for modeling heterogeneous outbreak distributions. Theoretical tractability enables clear inference; simulations validate estimator behavior over realistic sample sizes; and real data from Aseer demonstrate consistent gains in both global and tail fit. With appropriate safeguards for temporal dependence and reporting noise, the model provides a practical, interpretable, and scalable component for modern epidemiological analytics.

7. Findings and Conclusions

This work advances a trigonometric-generated family of distributions sub-model—the NewWeibull distribution—from first principles to practice. The mathematical development supplies tractable moment formulas (raw and central), conditions that justify series–integral interchange, and regularity results for maximum-likelihood estimation. These imply identifiability and the usual large sample guarantees for $(\hat{k}, \hat{\eta})$. A Monte Carlo study then verifies theoretical predictions across realistic sample sizes, and a city-level analysis of COVID-19 daily cases from the Aseer Region demonstrates consistent gains over classical competitors.

From the simulation evidence (Tables 11–15; Figures 14–15), the estimator of the scale parameter is effectively unbiased across all designs, with standard deviations contracting at the expected $n^{-1/2}$ rate and biases becoming numerically negligible by $n \geq 1000$ (often $\leq 7 \times 10^{-4}$). The shape estimator shows a small positive bias at exceedingly small n that diminishes rapidly and typically crosses zero near $n \approx 1000$. MSEs decline monotonically: for example, with $\eta = 1.5$ the MSE drops from 0.0697 at $n = 50$ to 0.00142 at $n = 2000$; with $k = 3.0$ it falls from 0.1163 to 0.00227 over the same range. A practical consequence is asymmetry in difficulty—η is easier to estimate than k at modest n—so precise inference on k benefits from windows of at least several hundred observations and simple stabilizers such as optimization on the log-scale.

Empirically, the NewWeibull provides the most favorable combination of global and tail fit across all examined cities, pairing low ADE and CVME with high KS p-values. In Ahad Rifaydah (Table 6; Figure 9), it attains CVME $\approx$ 0.028 and KS p $\approx$ 0.989 with the smallest ADE ($\approx$ 0.189), while the SinWeibull distribution severely overfits (ADE $>$ 4.5, KS p $\approx$ 0.004). In Billasmar (Table 7; Figure 10), where tails are heaviest, NewWeibull distribution again leads on the joint criteria, whereas the Exponential and Sin Weibull distributions deteriorate sharply on CVME and ADE. Sarat Abidah (Table 8; Figure 11) exhibits surge-prone behavior; NewWeibull distribution maintains tail control (ADE $\approx$ 0.500; CVME $\approx$ 0.068) with competitive KS. Al Harajah (Table 9; Figure 13) is shorter and more

skewed; NewWeibull distribution delivers the most balanced trade-off (CVME ≈ 0.067; KS p ≈ 0.79). In Abha (Table 10; Figure 12), representing concentrated urban transmission, it achieves CVME ≈ 0.0435 and ADE ≈ 0.2893 with KS p ≈ 0.9711, improving on the nearest competitor in both global and tail metrics. These outcomes align with the descriptive contrasts in Table 5, where right-skew and tail heaviness vary sharply by city.

The hazard-rate function behavior inferred from fitted parameters explains these gains. With two interpretable controls, the NewWeibull distribution reproduces early-onset bursts, transitional stabilization, and late-escalation patterns within a single parametric family, avoiding ad hoc mixtures while retaining epidemiological interpretability. In practice, this supports clear narratives for volatile settings (e.g., Billasmar), surge-prone regimes (Sarat Abidah), and steadier profiles (Al Harajah), while delivering tight fits in a large urban center (Abha).

The study also provides a usable pathway to application. An interactive Shiny tool enables real-time fitting, visualization, and model comparison without specialized coding, making the method accessible to analysts and public-health teams. The simulation results indicate that routine surveillance lengths already place $\hat{\eta}$ in the asymptotic regime, and that reliable inference for k is feasible once rolling windows reach several hundred observations—practical guidance for scheduling re-fits and forming confidence intervals.

Two limitations merit acknowledgement. First, the present analysis targets marginal distributions of daily counts; it does not model serial dependence or reporting artifacts directly. Standard safeguards—autocorrelation checks, detrending or mean-process modeling before distributional fitting, and bootstrap/profile-likelihood intervals—should accompany deployment. Second, while the Sin Weibull distribution instability cautions against unconstrained flexibility, there are contexts where mixtures or covariate-indexed parameters may be preferable; this is a deliberate parsimony–expressiveness trade-off.

In conclusion, the NewWeibull distribution is mathematically transparent, statistically well-behaved, and empirically effective for heterogeneous outbreak distributions. Theory clarifies inference; simulations validate estimator performance over realistic sample sizes; and city-level evidence from Aseer shows consistent advantages in both global and tail fit. With routine diagnostics for temporal dependence and reporting noise, the model constitutes a practical, interpretable, and scalable component for modern epidemiological analytics, and it extends naturally to survival, reliability, and chronic-disease settings where flexible hazard structures are essential.

Conflict of Interest: The authors show there is no conflict on interests.

Data availability Statement: We sourced the COVID-19 case data from the KAPSARC Data Portal and are shared in Appendix A.1.

Ethics Approval declaration: Not applicable. The study uses publicly available COVID-19 data and does not involve human participants.

Funding: Not applicable. This research received no external funding. The funding body had no role in the study design, analysis, interpretation of data, or writing of the manuscript.

Author Contributions Statement: A.A. and M.Z.A. jointly conceived the research idea, designed the study framework, and developed the methodological foundation. Both authors contributed to data preprocessing, exploratory analysis, probabilistic modeling, and development of machine-learning components. All computational experiments, including stability analysis, run-time evaluation, and model validation, were performed by both authors. A.A. and M.Z.A. generated all figures, tables, and visualizations, interpreted the analytical findings, and prepared the manuscript. Both authors critically reviewed the manuscript for intellectual rigor and approved the final version for submission.

References

1. Sindhu, T.N.; Atangana, A. Reliability Analysis Incorporating Exponentiated Inverse Weibull Distribution and Inverse Power Law. *Qual. Reliab. Eng. Int.* **2021**, *37*, 2399–2422.

2. Liu, X.; Ahmad, Z.; Gemeay, A.M.; Abdulrahman, A.T.; Hafez, E.H.; Khalil, N. Modeling the Survival Times of the COVID-19 Patients with a New Statistical Model: A Case Study from China. *PLoS ONE* **2021**, *16*, e0254999.
3. Shen, Z.; Alrumayh, A.; Ahmad, Z.; Abu-Shanab, R.; Al-Mutairi, M.; Aldallal, R. A New Generalized Rayleigh Distribution with Analysis to Big Data of an Online Community. *Alex. Eng. J.* **2022**, *61*, 11523–11535.
4. Moccia, B.; Mineo, C.; Ridolfi, E.; Russo, F.; Napolitano, F. Probability Distributions of Daily Rainfall Extremes in Lazio and Sicily, Italy, and Design Rainfall Inferences. *J. Hydrol. Reg. Stud.* **2021**, *33*, 100771.
5. Chen, P.; Ye, Z.S. Estimation of Field Reliability Based on Aggregate Lifetime Data. *Technometrics* **2017**, *59*, 115–125.
6. Xu, A.; Zhou, S.; Tang, Y. A Unified Model for System Reliability Evaluation under Dynamic Operating Conditions. *IEEE Trans. Reliab.* **2019**, *70*, 65–72.
7. Zhang, L.; Xu, A.; An, L.; Li, M. Bayesian Inference of System Reliability for Multicomponent Stress-Strength Model under Marshall–Olkin Weibull Distribution. *Systems* **2022**, *10*, 196.
8. Luo, C.; Shen, L.; Xu, A. Modelling and Estimation of System Reliability under Dynamic Operating Environments and Lifetime Ordering Constraints. *Reliab. Eng. Syst. Saf.* **2022**, *218*, 108136.
9. Zhuang, L.; Xu, A.; Wang, X.L. A Prognostic Driven Predictive Maintenance Framework Based on Bayesian Deep Learning. *Reliab. Eng. Syst. Saf.* **2023**, *234*, 109181.
10. Bantan, R.A.; Chesneau, C.; Jamal, F.; Elbatal, I.; Elgarhy, M. The Truncated Burr XG Family of Distributions: Properties and Applications to Actuarial and Financial Data. *Entropy* **2021**, *23*, 1088.
11. Reyad, H.; Korkmaz, M.C.; Afify, A.Z.; Hamedani, G.G.; Othman, S. The Fréchet Topp Leone-G Family of Distributions: Properties, Characterizations and Applications. *Ann. Data Sci.* **2021**, *8*, 345–366.
12. Eghwerido, J.T.; Agu, F.I. The Shifted Gompertz-G Family of Distributions: Properties and Applications. *Math. Slovaca* **2021**, *71*, 1291–1308.
13. Eghwerido, J.T.; Nzei, L.C.; Omotoye, A.E.; Agu, F.I. The Teissier-G Family of Distributions: Properties and Applications. *Math. Slovaca* **2022**, *72*, 1301–1318.
14. Altun, E.; Alizadeh, M.; Yousof, H.M.; Hamedani, G.G. The Gudermannian Generated Family of Distributions with Characterizations, Regression Models and Applications. *Stud. Sci. Math. Hung.* **2022**, *59*, 93–115.
15. Kumar, D.; Singh, U.; Singh, S.K. A New Distribution Using Sine Function—Its Application to Bladder Cancer Patients' Data. *J. Stat. Appl. Probab.* **2015**, *4*, 417.
16. Alharbi, R. Probabilistic Modeling of COVID-19 Events: Exploring New Alpha Generated Family for Enhanced Analysis Capabilities. *Alex. Eng. J.* **2024**, *94*, 287–309.
17. Gonçalves, L.; Turkman, M.A.A.; Geraldes, C.; Marques, T.A.; Sousa, L. COVID-19: Nothing Is Normal in This Pandemic. *J. Epidemiol. Glob. Health* **2021**, *11*, 146–149.
18. Ahmad, Z.; Almaspoor, Z.; Khan, F.; El-Morshedy, M. On Predictive Modeling Using a New Flexible Weibull Distribution and Machine Learning Approach: Analyzing the COVID-19 Data. *Mathematics* **2022**, *10*, 1792.
19. Farooq, M.; Ijaz, M.; Atif, M.; Abushal, T.; El-Morshedy, M. Statistical Analysis of COVID-19 Mortality Rate via Probability Distributions. *PLoS ONE* **2022**, *17*, e0274133.
20. Ahsan-ul-Haq, M.; Ahmed, M.; Zafar, J.; Ramos, P.L. Modeling of COVID-19 Cases in Pakistan Using Lifetime Probability Distributions. *Ann. Data Sci.* **2022**, *9*, 141–152.
21. Xin, Y.; Zhou, Y.; Mekiso, G.T. A New Generalized-Family for Analyzing the COVID-19 Data Set: A Case Study. *Math. Probl. Eng.* **2022**, 1–10.
22. Arif, M.; Khan, D.M.; Aamir, M.; Khalil, U.; Bantan, R.A.; Elgarhy, M. Modeling COVID-19 Data with a Novel Extended Exponentiated Class of Distributions. *J. Math.* **2022**, 1–14.
23. Ahmadini, A.A.H.; Elgarhy, M.; Shawki, A.W.; Baaqeel, H.; Bazighifan, O. Statistical Analysis of the People Fully Vaccinated against COVID-19 in Two Different Regions. *Appl. Bionics Biomech.* **2022**, 1–12.

24. Alsuhabi, H.; Alkhairy, I.; Almetwally, E.M.; Almongy, H.M.; Gemeay, A.M.; Hafez, E.H.; Sabry, M. A Superior Extension for the Lomax Distribution with Application to COVID-19 Infections Real Data. *Alex. Eng. J.* **2022**, *61*, 11077–11090.
25. BuHamra, S.S.; Al-Kandari, N.M.; Hussam, E.; Almetwally, E.M.; Gemeay, A.M. A Case Study for Kuwait Mortality during the Consequent Waves of COVID-19. *Heliyon* **2024**, *10*, e25953.
26. Tashkandy, Y.A.; Almetwally, E.M.; Ragab, R.; Gemeay, A.M.; Abd El-Raouf, M.M.; Khosa, S.K.; Bakr, M.E. Statistical Inferences for the Extended Inverse Weibull Distribution under Progressive Type-II Censored Sample with Applications. *Alex. Eng. J.* **2023**, *65*, 493–502.
27. Riad, F.H.; Alruwaili, B.; Gemeay, A.M.; Hussam, E. Statistical Modeling for COVID-19 Virus Spread in Kingdom of Saudi Arabia and Netherlands. *Alex. Eng. J.* **2022**, *61*, 9849–9866.
28. Bantan, R.A.; Chesneau, C.; Jamal, F.; Elgarhy, M. On the Analysis of New COVID-19 Cases in Pakistan Using an Exponentiated Version of the M Family of Distributions. *Mathematics* **2020**, *8*, 953.
29. Alshanbari, H.M.; Odhah, O.H.; Almetwally, E.M.; Hussam, E.; Kilai, M.; El-Bagoury, A.A.H. Novel Type I Half Logistic Burr–Weibull Distribution: Application to COVID-19 Data. *Comput. Math. Methods Med.* **2022**, *2022*, 1444859.
30. Almetwally, E.M.; Abdo, D.A.; Hafez, E.H.; Jawa, T.M.; Sayed-Ahmed, N.; Almongy, H.M. The New Discrete Distribution with Application to COVID-19 Data. *Results Phys.* **2022**, *32*, 104987.
31. Aljohani, H.M.; Ahsan-ul-Haq, M.; Zafar, J.; Almetwally, E.M.; Alghamdi, A.S.; Hussam, E.; Muse, A.H. Analysis of COVID-19 Data Using Discrete Marshall–Olkinin Length Biased Exponential: Bayesian and Frequentist Approach. *Sci. Rep.* **2023**, *13*, 12243.
32. Raihen, M.N.; Akter, S.; Tabassum, F.; Jahan, F.; Begum, S. A Statistical Analysis of Excess Mortality Mean at COVID-19 in 2020–2021. *Comput. J. Math. Stat. Sci.* **2023**, *2*, 223–239.
33. Faruk, M.U.; Isa, A.M.; Kaigama, A. Sine–Weibull Distribution: Mathematical Properties and Application to Real Datasets. *Reliab. Theory Appl.* **2024**, *19*, 65–72.
34. Elbatal, I.; Alotaibi, N.; Al-Dayel, I.; Shawki, A.W.; Elgarhy, M. Statistical Analysis of COVID-19 Data in Kingdom of Saudi Arabia Using Sine Modified Weibull Model. *JP J. Biostat.* **2022**, *20*, 11–26.
35. Ogumeyo, S.A.; Opone, F.C.; Abubakari, A.G.; Ehiwario, J.C. A Bounded Lifetime Distribution Specified by a Trigonometric Function: Properties, Regression Model, and Applications. *Int. J. Math. Math. Sci.* **2024**, *2024*, 5583105.
36. Kumar, P.; Sapkota, L.P.; Kumar, V.; Tashkandy, Y.A.; Bakr, M.E.; Balogun, O.S.; Gemeay, A.M. A New Class of Cosine Trigonometric Lifetime Distribution with Applications. *Alex. Eng. J.* **2024**, *106*, 664–674.
37. Mahmood, Z.; Khogeer, H.A.; Hussam, Hafez, E.; Hossain, M.M. A Logistic Trigonometric Generalized Class of Distribution Characteristics, Applications, and Simulations. *J. Math.* **2022**, *2022*, 7091581.
38. Tashkandy, Y.A.; Elshenawy, A.; Tekle, G.M.; Bakr, M.E.; Balogun, O.S. A Novel Distributional Approach Based on the Trigonometric Function with Medical Data Sets. *Alex. Eng. J.* **2024**, *96*, 303–322.
39. Souza, L. New Trigonometric Classes of Probabilistic Distributions. Ph.D. Thesis, Universidade Federal Rural de Pernambuco,Recife, Brazil, **2015**.

Appendix A.1

Application 1: Daily COVID-19 cases in Ahad Rifaydah, Aseer Region, Saudi Arabia, from May 31 to September 1, 2020.

1, 18, 13, 9, 9, 23, 62,11, 45, 5, 44, 15, 5, 7, 36, 11, 31, 38, 23, 15, 9, 4, 6, 3, 31, 1.

Application 2: Daily COVID-19 cases in Billasmar, Aseer Region, Saudi Arabia, from June 1, 2020, to January 21, 2022.

2, 4, 11, 6, 9, 13, 9, 6, 5, 2, 16, 25, 12, 21, 21, 1, 66, 15, 8, 19, 25, 16, 9, 5, 4, 2, 1, 4, 2, 12, 7, 1, 4, 5, 12, 2, 3, 8, 9, 8, 5, 3, 4, 18, 15, 17, 21, 13, 35, 3, 3, 15.

Application 3: Daily COVID-19 cases in Sarat Abidah, Aseer Region, Saudi Arabia, from June 29 to July 25, 2020.

1, 16, 2, 11, 6, 11, 7, 3, 15, 7, 25, 7, 3, 2, 18, 19, 2, 6, 5, 40,9, 2, 14, 1, 20, 2, 25, 30,19, 42, 16, 6, 3, 11, 3, 72, 11, 7, 11, 1, 3, 19, 8, 12, 7.

Application 4: Daily COVID-19 cases in Al Harajah, Aseer Region, Saudi Arabia, from July 2 to August 15, 2020.

2, 5, 3, 6, 1, 3, 17, 7, 7, 2, 14, 33, 21, 17, 8, 18, 35, 9, 23, 2, 7, 1, 1, 1, 2.

Application 5: Daily COVID-19 cases in Abha, Aseer Region: from May 7th, 2021 to June 30th, 2021.

15, 19, 10, 15, 17, 4, 9, 7, 13, 28, 42, 41, 32, 25, 39, 45, 32